Modelling water temperature dynamics for eelgrass (*Zostera marina*) areas in the nearshore Scotian Shelf

Aidin Jabbari[1,a*], Yongsheng Wu[1], Melisa Wong[1], Mike Dowd[2]

[1] *Fisheries and Oceans Canada, Bedford Institute of Oceanography, Dartmouth, Nova Scotia B2Y 4A2 Canada*

[2] *Department of Mathematics and Statistics, Dalhousie University, Halifax, Nova Scotia B3H 4R2 Canada*

[a] *Present address: National Institute of Water and Atmospheric Research, Christchurch 8440, New Zealand*

[*] Corresponding author

E-mail address: Aidin.Jabbari@niwa.co.nz

Abstract

Water temperature is an important environmental factor for the growth of eelgrass (*Zostera marina*) beds, which provide important nearshore ecosystem services. Here, we study water temperature dynamics in eelgrass beds off the Atlantic coast of Nova Scotia using a high-resolution nearshore oceanographic model based on the Finite Volume Community Ocean Model (FVCOM). The model has been evaluated against the observed temperature at six sites for three years from 2017-2019; the evaluation indicates that the model is able to replicate the temperature variation on time scales from hours to seasonal. We also use various temperature metrics relevant to eelgrass condition, including mean seasonal values and variability, daily ranges, growing degree day, and warm events, to both validate the model and better understand the temperature regime at the study sites. Our analyses showed that eelgrass inhabit a wide range of temperature conditions that have previously been shown to influence their performance. The mean water temperature during the summer growing period differs by more than 7°C between the shallowest and the deepest sites. The rate of heat accumulation was faster at shallow sites, and they experienced ≥ 12 extreme warm events year^{-1}. While the amplitude of the temperature variations within the high frequency band (<48 hr) was greater in shallower sites, temperature changes on meteorological time scales (48 hr to 60 days) were coherent at all sites suggesting the importance of coast-wide processes. The results of this study demonstrate that our high resolution numerical model can capture biologically relevant temperature dynamics at different time scales and over a large spatial region and yet still capture detailed temperature dynamics at specific nearshore sites. It therefore has the potential to contribute to conservation planning and prediction of eelgrass response to future climate changes.

1 Introduction

Nearshore temperature dynamics can be highly heterogeneous both spatially and temporally, due to the complex interplay of air-sea heat fluxes with localized geometry, atmospheric forcings that influence water currents and mixing, and its interaction with shelf and deep ocean physical processes. In turn, these highly variable temperature regimes have potentially significant effects on valued ecosystem components, including eelgrass (*Zostera marina*) beds. Eelgrass, like other seagrass species, provides important ecosystem services such as shoreline protection, water filtration, carbon storage, and fisheries maintenance (Fourqurean et al., 2012; Nordlund et al. 2016). While temperature, light, and nutrients all influence eelgrass growth and production (Lee et al. 2007), temperature is a particularly important driver within the context of climate change. Previous work has shown that temperature effects on eelgrass are multi-faceted, with multiple short-term (i.e., seasonal and sub-seasonal) temperature processes acting concomitantly (Krumhansl et al. 2021). Eelgrass productivity and resilience tends to be lower in warm and highly variable temperature regimes where heat accumulates quickly and thermal physiological thresholds are exceeded (Krumhansl et al. 2021, Wong and Dowd 2023). Furthermore, eelgrass is also susceptible to marine heatwaves that originate offshore but propagate into, and are exacerbated by, nearshore conditions (Marbà and Duarte, 2010; Moore et al., 2014; Strydom et al. 2020; Wiberg, 2023). Understanding the relationship of eelgrass distribution and condition with the physical environment requires high resolution physical data across large spatial scales. Unfortunately, it is not feasible to obtain this information from *in-situ* measurements or satellite data due to limitations in data resolution and spatial scales. Hence, we must rely on properly calibrated and validated numerical ocean models. Despite advances in oceanographic model developments, predicting temperature accurately and capturing its variability on the small spatial

and temporal scales characteristic of the nearshore is difficult. Furthermore, model predictions are most useful if they are evaluated using ecologically meaningful temperature metrics that are linked to seagrass performance.

Our study region is the Atlantic coast of Nova Scotia, Canada. Water temperature over the Scotian Shelf has strong spatial and seasonal variability, with the main controlling mechanism being the air-sea heat flux (sum of the flux of solar heating, sensible heat, latent heat and longwave radiation) that accounts for about 85% of the observed temperature variability (Umoh and Thompson 1994). Cold water upwelling yields an important temperature signal in summer, and horizontal advection and the vertical mixing have relatively smaller contributions. Additionally, large scale variations in water temperature over the Scotian Shelf are related to the two dominant equatorward flows over the Scotian Shelf (Thompson et al. 1988; Petrie 2007; Brickman et al., 2018). The first is the inner-shelf current along the Atlantic coast, fed by a branch of the outflow from Gulf of St. Lawrence; and the second is the current along the shelf break, that is an extension of the Labrador Current (Sutcliffe et al., 1976). The two seasonally varying currents are topographically steered by banks, basins and channels, leading to variations in water temperature (Petrie and Drinkwater, 1993; Hannah et al., 1996; Drinkwater 1996; Wu et al., 2016).

Numerical models of the physical oceanography in this region have emphasized the Scotian Shelf, but largely ignored the nearshore due to the difficulty in adequately resolving it. During the last four decades, numerical models have been developed for the Scotian Shelf based on various types of circulation models with different model resolutions. For example, using finite element models, Han et al. (1997) and Hannah et al. (2001) investigated the seasonal variation of the circulation over the shelf with model resolution that varied from 2 km over the coastal waters

92 to 30 km in the deep ocean. Using a nested-grid modelling system, Sheng et al. (2006) studied
93 the response of the upper ocean to storms using a model resolution over the shelf of about 7 km.
94 Using an ice-ocean coupled model based on the Princeton Ocean Model, Wu et al. (2012)
95 developed a circulation model with a horizontal resolution of about 10 km, while Katavouta et al.
96 (2016) developed an ocean circulation model based on the Nucleus for European Modeling of
97 the Ocean (NEMO) with a horizontal resolution of 2.8 km. These models represent well the key
98 dynamics driving large-scale temperature variations over the Scotian Shelf, but cannot accurately
99 represent nearshore processes due to the relatively coarse model resolution used. More recently,
100 Feng et al. (2022) developed a model based on the Finite Volume Community Ocean Model
101 (FVCOM) for the eastern shore island area of the Scotian Shelf, however the spatial variation of
102 water temperatures in the target eelgrass areas in this study were still not adequately resolved.
103 The challenge to accurately modelling the nearshore temperature is the complicated bathymetry
104 and coastlines. This requires spatial resolution down to a few meters to achieve reasonable
105 temperature predictions, and to accurately represent the nearshore dynamics (Lynge et al., 2010;
106 McWilliams, 2016; Poje et al., 2010).

107 The eelgrass areas in this study are characterized by irregular coastlines, deep bays with
108 steep shorelines, shallow bays with elevated intertidal flats and tidal channels, and many islands
109 and headlands with strong tidal flows. Consequently, these eelgrass beds inhabit a wide range of
110 environmental conditions, from shallow, warm, protected waters to deep, cool, exposed waters
111 (Wong 2018, Krumhansl et al. 2021). Eelgrass beds also experience high temporal variability in
112 water temperature from not only localized processes such as air-sea heat fluxes (i.e., local
113 forcing), but also tidal and wind driven advective heat fluxes originating on the shelf (i.e., remote
114 forcing) (Wong et al., 2013; Wong and Dowd, 2021). To understand the dynamics of water

temperature in the eelgrass areas, in this study we develop a high resolution numerical oceanographic model which uses an unstructured mesh that allows for very high spatial resolutions at sites of interest. This allows us to represent the complex coastline and bathymetry and to provide accurate water temperature predictions where needed, such as in shallow eelgrass beds ventilated by only a few channels. Using the model results, we examine ecologically meaningful temperature metrics (i.e., mean temperature, heat accumulation, daily temperature range, thermal physiological threshold exceedances) that are known to influence seagrass growth and productivity (Krumhansl et al. 2021, Wong and Dowd 2023). Finally, a simple heat budget is developed to identify the primary mechanisms underlying the temperature dynamics at select study sites.

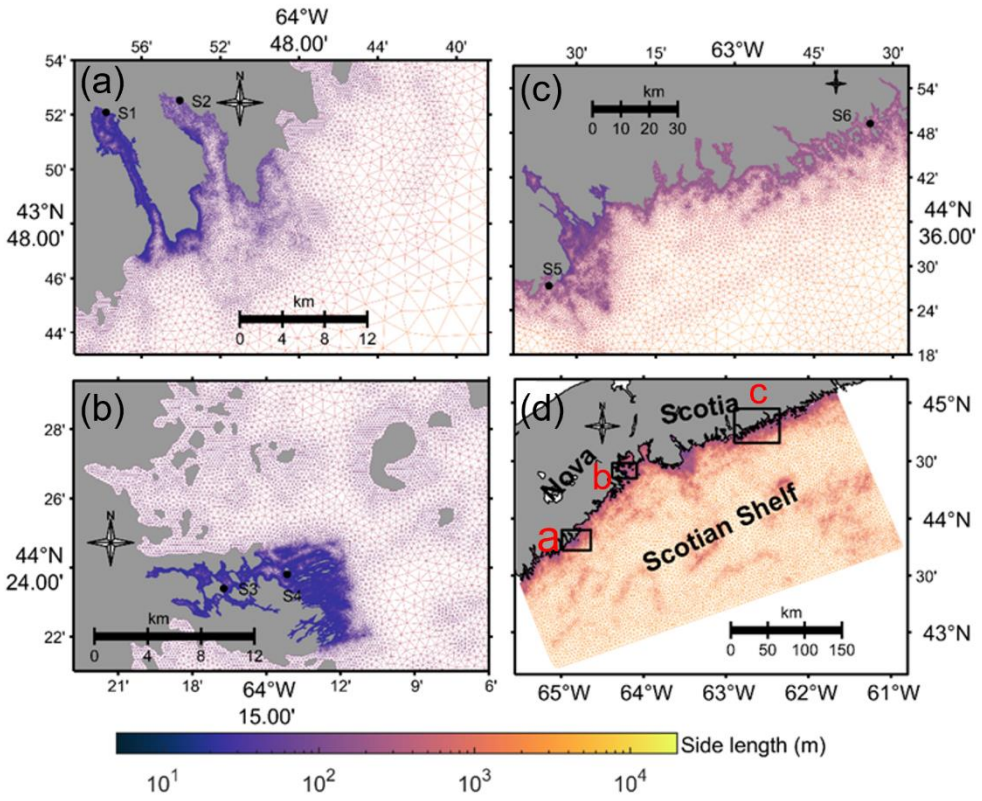

Fig. 1 Map showing the model domain and the computational mesh, along with the eelgrass study sites: Model domain (d) and details of the model mesh resolutions for core study areas (a-c). The locations of all study sites are the sites listed in Table 1. The designations S1-S6 refer to Port l'Hebert, Port Joli, Mason's Island, Sacrifice Island, Sambro, and Taylor Head, respectively.

2 Materials and methods

2.1 Model configuration

The ocean model used in this study is the FVCOM, which is a finite-volume, unstructured grid ocean model (Chen et al., 2007, 2003). The model has a free surface, uses sigma coordinates in the vertical direction, and employs a mode time split. FVCOM solves the three-dimensional momentum, continuity, temperature and salinity equations by computing fluxes between unstructured triangular elements. The unstructured mesh system in the model is able to fit

complex coastlines and enables a seamless transition between small-scale processes in eelgrass areas and large-scale processes in the adjacent shelf and open ocean, while maintaining computational efficiency. The model domain and model grid size are shown in Fig. 1. The model mesh includes 176755 nodes and 335819 elements. The horizontal resolution of the model mesh varies from 1-2 km in the open shelf to 10 m in the near-shore waters. An example of where locally very high resolution is important is Port l'Hebert, where the water temperature is strongly associated with the water advection through a narrow channel with the width less than 100 m (Fig. 1a).

The model bathymetry is based on high resolution survey data (10 m in our study areas) from the Canadian Hydrographic Service (CHS), which is mildly smoothed in order to reduce sigma-coordinate pressure gradient errors. The water column is divided into 30 layers in the vertical. For water depths shallower than 60 m, the sigma levels are uniformly distributed through the water column. For water depths deeper than 60 m, we used a generalized coordinate system to resolve the bottom boundary layer and to reduce the horizontal pressure gradient error: 10 uniform layers in the surface layer with an interval of 2 m, 5 uniform layers in the bottom layer with a 2 m interval, and 15 levels stretched to span the center of the water column. Vertical turbulent mixing is modelled with the General Ocean Turbulence Model (GOTM) using a k-ε formulation (Umlauf and Burchard, 2005), and the horizontal diffusion is parameterized as the Smagorinsky diffusivity with a coefficient of 0.1.

The temperature and salinity of the model are initialized from the daily reanalysis results of GLORYS12v1 with 1/12° resolution (Jean-Michel et al., 2021). The open boundary conditions employ a one-way nesting scheme with variables (water elevations, temperature, salinity and currents) from GLORYS12v1. The tidal components are also included through the

nesting; the tidal water elevations and tidal currents of eight major tidal constituents (M2, S2, N2, K2, O1, K1, P1, and Q1) are from the tidal dataset of TPXO9 (Egbert et al., 1994; Egbert and Erofeeva, 2002). Surface atmospheric forcing consists of wind at 10 m above the ocean surface, air temperature at 2 m, relative humidity at 2 m, precipitation, evaporation, shortwave radiation, and longwave radiation. We obtained these forcings with 1/4° resolution from ERA5 reanalysis datasets from the European Centre for Medium-Range Weather Forecasts. The FVCOM model as configured above outputted hourly 3D total currents, temperature, and sea level for the period of 2016 – 2022.

2.2 *In-situ* observations for model validation

Bottom water temperature and water pressure (i.e., sea level) were recorded at six eelgrass sites along the Atlantic coast of Nova Scotia, Canada (Figure 1, Table 1). These sites represent a range of environmental conditions over which eelgrass beds occur, including gradients of temperature, light, sediment properties, and water movement, all influenced by tidal currents, winds, waves, and bathymetry (Bakirman and Gumusay, 2020; Krumhansl et al., 2020; Wong and Dowd, 2021, Krumhansl et al. 2021). Port l'Hebert, Port Joli, and Mason's Island are the shallower sites (mean depth at high tide < 2 m) with muddy/silty sediments, low current speed, and low exposure to waves and offshore processes (Table 1, Fig.1). Other beds (Sacrifice Island, Taylor Head, and Sambro) were located in deeper water (mean depth at high tide > 3 m), with sandy sediments, higher current speeds, and higher exposure to waves and offshore dynamics (Table 1, Fig.1) (Krumhansl et al., 2020; Wong and Dowd, 2020).

Water depth was calculated from water pressure measurements made at 10 cm above the bed at 10 minutes intervals using HOBO pressure sensors (Onset Corp) during 24 July 2020 to 24 November 2021, and used for observing sea level variation. We used the water temperature

182 records by HOBO tidbit temperature loggers (Onset Corp) at 10 cm above the bed and logged
183 data every 15 minutes from 1 June 2018 to 31 October 2021, and used these data for model
184 validation. The observed data were generally recorded continuously although some logistical
185 challenges resulted in shorter deployments at some sites (Table 1). All the loggers were placed
186 directly in the eelgrass beds to record the actual conditions that the eelgrass experiences. At
187 some shallow sites, this meant that loggers were periodically exposed to the air at very low tides,
188 as were the seagrass beds. Temperature recordings from exposure were thus sometimes higher
189 (>30 ºC) and lower (below freezing) than expected if the loggers had remained submerged.
190 Extreme air temperatures have been shown to impact seagrasses (Park et al. 2016), so we elected
191 to retain these temperatures.
192

Table 1 Location, mean depth, and the period of observations at the six eelgrass sites.

Site	Lat.	Lon.	Mean depth at high tide (m)	Observed water depth period	Observed water temperature period
Port l'Hebert	43.8681	-64.9633	1.82	24/06/2021 to 24/10/2021	01/06/2018 to 20/03/2020 and 26/05/2020 to 31/05/2021
Port Joli	43.8754	-64.9009	1.59	24/06/2021 to 24/10/2021	01/06/2018 to 19/02/2019 and 18/04/2019 to 24/10/2021
Mason's Island	44.3899	-64.2788	1.91	24/06/2021 to 24/10/2021	01/06/2018 to 27/03/2019 and 06/05/2019 to 31/10/2021
Sacrifice Island	44.3967	-64.2360	3.28	24/06/2021 to 24/10/2021	01/06/2018 to 04/02/2019 and 06/05/2019 to 31/10/2021
Sambro	44.4554	-63.5879	6.36	24/06/2021 to 24/10/2021	01/06/2018 to 25/04/2019 and 15/08/2020 to 08/12/2020 and 16/06/2021 to 31/10/2021
Taylor Head	44.8205	-62.5719	3.89	24/06/2021 to 24/10/2021	10/06/2018 to 31/10/2021

193

194 2.3 Analyses

195 2.3.1 Tidal analysis of sea level

196 The tidal components of sea level from FVCOM are compared to those from sea level records at
197 the eelgrass sites for five selected dominant principal tidal constituents (O1, K1, N2, M2, and S2
198 with periods of 25.84 hr, 23.92 hr, 12.66 hr, 12.42 hr, 12.00 hr, respectively), four overtides (M4,
199 S4, M6, and M8 with periods of 6.21 hr, 6.00 hr, 4.14 hr, 3.11 hr, respectively), and one
200 compound tide (2MK5 with period of 4.93 hr) with a signal-to-noise ratio greater than 2. The
201 amplitudes and phases of the tidal constituents are calculated using the T-Tide toolbox of
202 Pawlowicz et al. (2002).

203 **2.3.2 Prediction of temperature variations**

204 The temperature time series from both the observations and model predictions were processed to
205 isolate signals in different frequency bands, specifically: (i) low frequency (changes occurring
206 over with periods > 60 days); (ii) middle frequency (changes that occur with periods ranging
207 from 48 hr to 60 days); and (iii) high frequency (temperature changes that occur with periods $\leq$
208 48 hr). Low frequency temperature changes are related to seasonal and annual cycles (on the
209 order of months to years). Middle frequency temperatures are associated with meteorological
210 events such as storms and wind driven upwelling events, or any processes with time scales of
211 days to weeks. High frequency temperature changes are usually related to tidal exchanges and
212 daily heating and cooling processes (period of 10 - 48 hr). Overtides also contribute to high
213 frequency temperature variation, and are usually harmonics of the principal tidal constituents
214 with periods of 3-10 hr. The analysis was carried out as follows. The low frequency (seasonal)
215 water temperature variations were isolated by fitting polynomial functions to the raw temperature
216 data at each site. The de-seasonalized time series (the temperature anomaly) were then calculated
217 by subtracting the seasonal cycle from the original temperature time series. A low-pass filter was
218 then applied to the temperature anomaly time series to remove the high frequency features (< 48

hr) and obtain the meteorological (mid frequency) band. The high frequency (tidal/daily) band was calculated by subtracting the meteorological band from the temperature anomaly.

Time series of the three different frequency bands at each site were compared for the observations and model predictions using the Willmott skill (WS), defined as:

$$WS = 1 - MSE/\langle(|m - \langle o\rangle| + |o - \langle o\rangle|)^2\rangle, \quad (1)$$

where $MSE = \langle(m - o)^2\rangle$ is the mean square error, *m* and *o* are time series of the modelled and observed variables, respectively, and $\langle \quad \rangle$ represents a mean. The highest (1) and lowest (0) values of WS show perfect agreement and complete disagreement between the model predictions and observations, respectively. This method has been used previously for assessment of numerical models for simulation of different parameters in aquatic environments (e.g., Liu et al., 2009; Warner et al., 2005; Wilkin, 2006). In addition to this frequency resolved WS, summary statistics of the bottom water temperature including mean, maximum, and minimum temperatures, standard deviation (SD), and the 95th percentile are used to compare the model predictions and observations.

2.3.3 Spectral analysis of water temperature

A power spectral analysis of the bottom water temperature at each site for both the observed data and model predictions was performed. These analyses help with identifying the dominant frequencies of the water temperature variation (e.g., diurnal tides, solar heating and cooling, semi-diurnal tides, overtides and compound tides in shallow waters), as well as assessing the capability of the model in computing them as compared to those found in the observations.

2.3.4 Eelgrass specific temperature metrics

Model accuracy in prediction of water temperature metrics ecologically relevant for eelgrass were also evaluated and include: growing degree days (GDD); warm water events that exceed physiological thresholds; and daily temperature range.

The thermal integral, known as growing degree days (GDD), has been used in horticulture and fish studies to predict growth and development (Neuheimer and Taggart, 2007). GDD quantifies heat accumulation over time in a system and has been shown to influence eelgrass productivity and resilience (Krumhansl et al., 2021, Wong and Dowd 2023). Here, GDD from model predictions and from in-situ observations is estimated by:

$$GDD(t) = \int_{t_0}^{t} max((T_{max} + T_{min})/2 - T_{base}, 0)dt \quad (2)$$

Where, when a full year of observed data available at all sites, T_{max} and T_{min} are the daily maximum and minimum temperature, respectively, and T_{base} is a prescribed base temperature. GDD is calculated for 01 June 2018 (t_0) to 25 April 2019 where almost a full year of observed data are available at all sites. Eelgrass photosynthesis increases rapidly from 0 to 5 °C, while a maximum in the ratio of photosynthesis to respiration (P:R) occurs at 5 °C (Biebl et al., 1971; Marsh et al., 1986). Therefore, we elected to use 5 °C as T_{base} in our calculations of GDD, as done previously in Krumhansl et al. (2021).

We also calculated the frequency and duration of warm water events that exceeded known physiological thermal thresholds for eelgrass using both the model predictions and the observed data. We used three different temperature thresholds (T_{th}) of 20 °C, 23 °C, and 27 °C. The 23 °C temperature is typically considered the physiological threshold for temperate eelgrass above which respiration begins to outpace photosynthesis, causing reduced or even negative P:R ratios that result in reduced eelgrass growth and survival (Lee et al., 2007). However, eelgrass is

highly adaptable, and plants in warm conditions likely have higher temperature thresholds while plants in cooler conditions have lower ones. We thus also used 20 °C and 27 °C as thresholds. Individual warm water events were identified as those occurring above the temperature thresholds for ≥ 2 hr, with distinct events separated by ≥ 3 days, akin to the definition for marine heatwaves (Krumhansl et al., 2021; Oliver et al., 2018).

Finally, to estimate the daily temperature range, the difference between the daily 90th and 10th percentiles are calculated and compared between the model predictions and observed data. The probability density of the daily temperature ranges are also calculated using kernel density estimation.

2.3.5 Nearshore heat balance

A simple heat budget is applied to the FVCOM model results to estimate the relative contributions of different processes that can contribute to the warming or cooling of the water in the immediate region around 2 selected eelgrass sites with different physical dynamics. Here the heat budget is applied following standard approaches for the coastal regions (Dever and Lentz, 1994; Lemagie et al., 2021, 2020). The heat budget in a generic form may be expressed as

$$\frac{\partial \bar{T}}{\partial t} = \frac{Q}{\rho C_p H} + \frac{1}{H}\int_{-H}^{0} \vec{u} \cdot \nabla T \, dz + \varepsilon \qquad (3)$$

where $\bar{T}$ is the mean temperature in the box surrounding the site extended to the shoreline (i.e., depth and laterally averaged water temperature), Q is the surface heat flux, ρ = 1024.6 kg m^{-3} is the reference density of seawater, C_P = 4002.5 J kg^{-1} °C^{-1} is its heat capacity, H is the depth, and $\vec{u}$ is the horizontal velocity. The left-hand side of Eq. 3 shows the rate of temporal change in the heat content, or temperature tendency, of the region (δT^{Avg}). The first term on the right-hand side is the heat flux through the surface (δT^{SHF}), and the second term estimates the advective

heat flux (δT^{Adv}). Finally, the last term is the residual of the balance (ε), which could be due to processes such as mixings, eddies, or other complex three-dimensional processes that were not captured by this simple heat budget. To evaluate the contribution of each term on the temperature change over the region, each term in Eq. 3 is expressed as an equivalent temperature change in units of °C hr^{-1}. The heat budget is also integrated over time to assess the variation of each term for different seasons.

3 Results

3.1 Sea level

Figure 2 shows the amplitude and phase of sea level for selected tidal constituents at Port l'Hebert and Taylor Head (selected as representative shallow and deep sites, respectively, with the remaining sites presented in Fig. S1). Of all the principal tidal constituents, the M2 tide has the largest amplitude (> 0.55 m) across all the sites. Shallower sites (Port l'Hebert (Fig. 2b), Port Joli (Fig. S1b), and Mason's Island (Fig. S1d)) are generally associated with higher amplitude of harmonic constituents than the deeper sites (Taylor Head (Fig. 2d), Sacrifice Island (Fig. S1j), and Sambro (Fig. S1l)). While there are differences between the modelled and observed phase for principal tidal constituents (< 30°) (Figs. 2e-h and S1e-h and S1m-p), the errors in prediction of amplitude and phases of the principal and harmonic tidal constituents are generally within the error standard deviation associated with their calculations (Figs. 2 and S1).

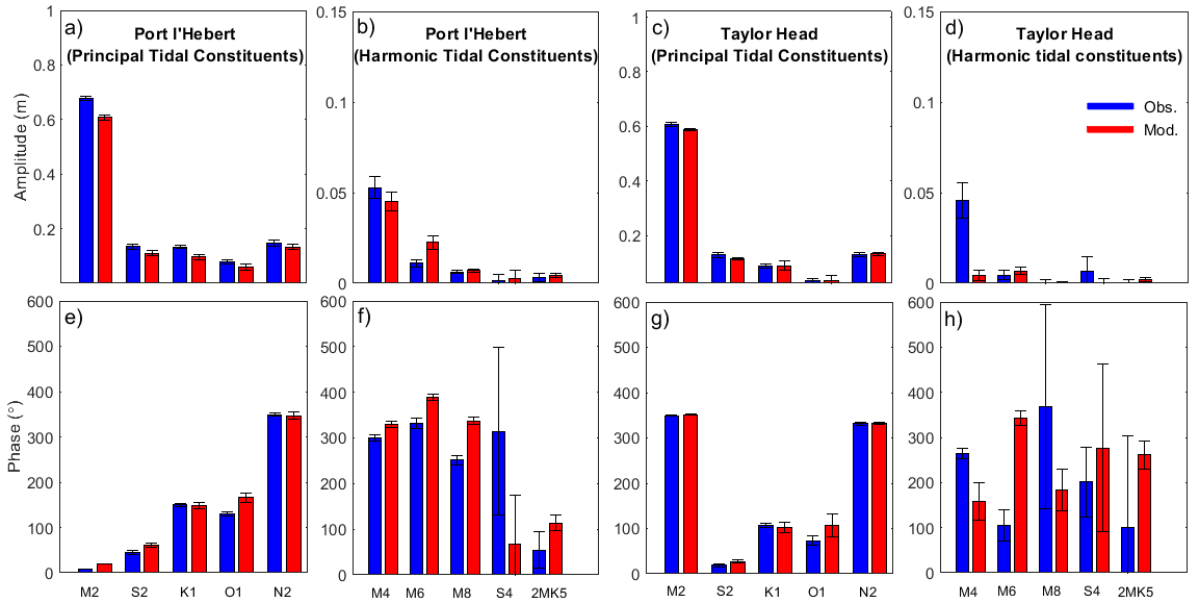

Fig. 2 Amplitude (top) and phase (bottom) of sea level for five select principal tidal constituents (M2, S2, K1, O1, and N2; panels a, e, c, and g) and five harmonic tidal components (M4, M6, M8, S4, and 2MK5; panels b, f, d, and h) from observed data (blue) and model results (red) for 2 select sites: Port l'Hebert, a shallow site (panels a, b, e, and f) and Taylor Head, a deep site (panels c, d, g, and h). Length of the error bars show the standard deviation.

303

304 ## 3.2 Water temperature variations

305 Comparison of the bottom water temperature from the model and observations (Figs. 3-4 and S2-
306 S5) shows that the model can predict the time series of the observed data, as well as the
307 temperature variations at different frequencies, with Willmott skill greater than 0.7 (Table 2). In
308 comparisons of the low frequency time series, the model consistently overestimates summer
309 water temperatures at Port l'Hebert (max 7.2 °C for the observed data (Figs. 3a) and 1.7-2.5 °C
310 for the of low frequency data (Figs. 3b)) and Port Joli (max 4.4 °C for the observed data (Figs.
311 S2a) and 0.5-3.1 °C for the low frequency data (Figs. S2b)), the two shallow sites. Note that
312 maximum discrepancies for the observed data at these sites are influenced by temperature spikes
313 associated with the sensors being exposed briefly to air (as noted above). In contrast, the model
314 underestimated summer water temperature at the deeper sites (Figs. 4a-b, S3a-b, S4a-b, and S5a-

b) with the maximum discrepancy of 6.6 °C at Sacrifice Island (Figs. S4a and b). The model predictions of time series of the middle and high frequency temperature variations were generally within 2 °C of those observed (Figs. 3c-d, 4c-d, S3c-d, S4c-d, and S5c-d), with the maximum discrepancies of 4.7 °C at Sambro (Figs. S5c-d).

Across all sites, the bottom water temperature showed a seasonal trend of increasing water temperature during the spring with a maximum in August, and declining throughout the fall to a winter minimum in February (Figs. 3-4 and S2-S5). The largest seasonal ranges (> 32 °C) were at Port l'Hebert and Port Joli with an observed summer maximum of 28.81°C and 29.57 °C, respectively, and a winter minimum of -3.97 °C and -3.89 °C, respectively (Table 3), again being influenced by air exposure of the recorders. The lowest seasonal range (22.14 °C) was observed at Sambro (Fig. S5a-b). Temperature changes within the meteorological band at Port l'Hebert (Fig. 3c) and Port Joli (Fig. S2c) were similar and did not show large inter-seasonal variations. The highest amplitude within the meteorological band (peaks usually > 1°C; SD > 1.7°C) was also calculated in these two sites relative to others, with minimum amplitudes (generally < 2°C; SD < 1°C) in Mason's Island (Fig. S3c) and Sacrifice Island (Fig. S4c). Large consistent drops (~6°C) in the meteorological band at Sambro (Fig. S5c) could be attributed to the high winds in fall.

As with the variations found in the meteorological band, the highest amplitudes of the temperature variations within the high frequency band were at Port l'Hebert (Fig. 3d) and Port Joli (Fig. S2d). Of the deeper sites, Mason's Island (Fig. S3d) and Sacrifice Island (Fig. S4d) show the highest and lowest amplitudes of variations, respectively. Inter-seasonal changes within the high frequency band were evident in all the sites with the highest amplitudes during June to September, which could be an indicator of increased heating and cooling related to solar heating

and tides during warmer periods, or due to the establishment of localized horizontal temperature gradients. The highest (8.0 °C) and the lowest (2.3 °C) values of the summer peaks in the high frequency band were in Port Joli and Sacrifice Island, respectively. The highest (1.05 °C) and the lowest (0.36°C) SD in the high frequency band from the model results were also obtained in Port Joli and Sacrifice Island, respectively (Table 3). The ratios of the standard deviation of the high frequency to meteorological band was less than 1 in all the sites from both the model results and observations (Table 3), which shows that the processes within the meteorological band can dominate the temperature dynamics at these eelgrass sites.

The model calculation of the summary statistics (time series during 01/06/2018 to 31/05/2021) of the bottom water temperature are within 2 °C of the observed data in most sites (Table 3). The warmest mean bottom water temperature was in Port l'Hebert and Port Joli (11.62 °C and 11.44 °C, respectively) and the coldest mean temperature was in Sambro and Taylor Head (7.37 °C and 7.89 °C, respectively) from the model calculations. The highest maximum temperature, the highest 95th percentile temperature, and the lowest minimum temperatures calculated from both the model and observed data were found at Port l'Hebert and Port Joli. These sites also have the highest standard deviation of the temperature, which is an indicator of having the highest temperature variations among all the sites.

Table 2 Average Willmott skill score for the bottom water temperature prediction decomposed by frequency. Here scores of 1 and 0 indicate perfect agreement and complete disagreement, respectively, between the model results and observations

Site	Time series	Low frequency (> 60 days)	Middle frequency (48 hr to 60 days)	High frequency (< 48 hr)
Port l'Hebert	0.98	0.99	0.92	0.81
Port Joli	0.99	0.99	0.93	0.79
Mason's Island	0.98	0.98	0.89	0.72
Sacrifice Island	0.96	0.96	0.83	0.77
Sambro	0.98	0.99	0.88	0.71
Taylor Head	0.98	0.99	0.91	0.77

355

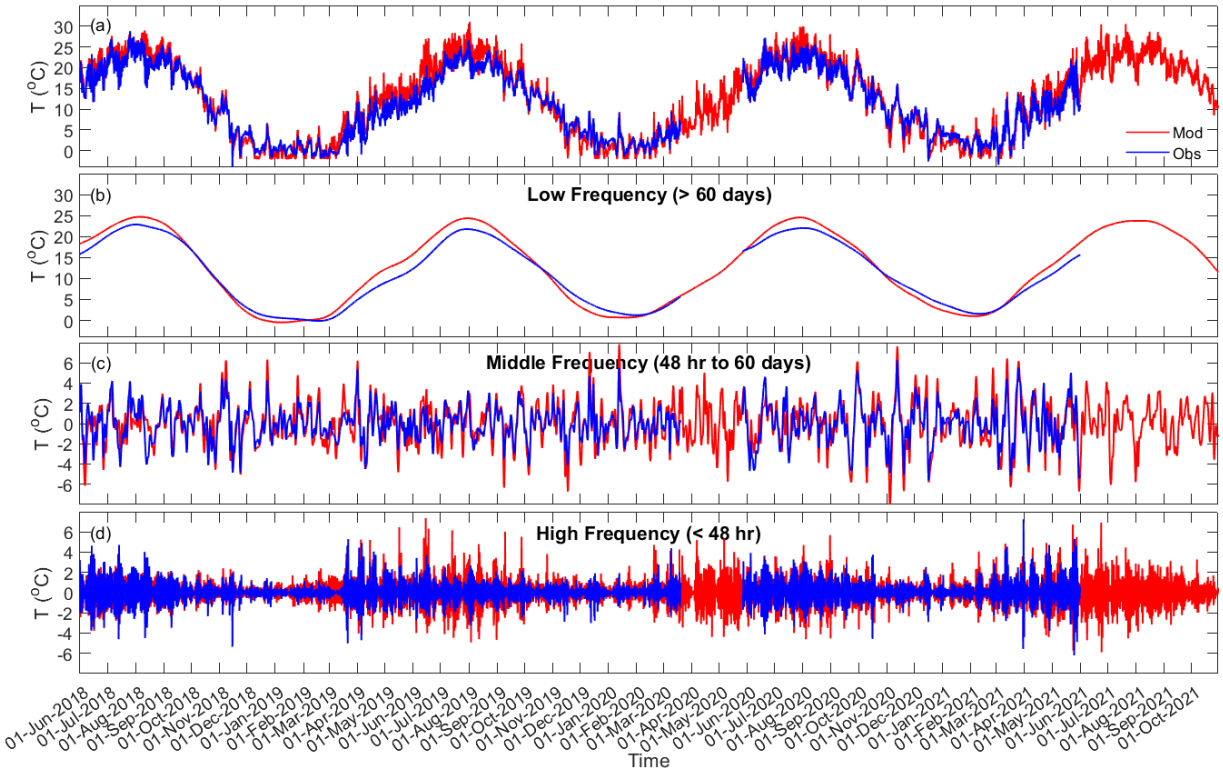

Fig. 3 Port l'Hebert bottom water temperature time series (a), and time series of the bottom water temperature in low (> 60 days (seasonal band); b), middle (48 hr to 60 days (meteorological band); c), and high (< 48 hr; d) frequencies from observation data (blue) and model results (red).

356

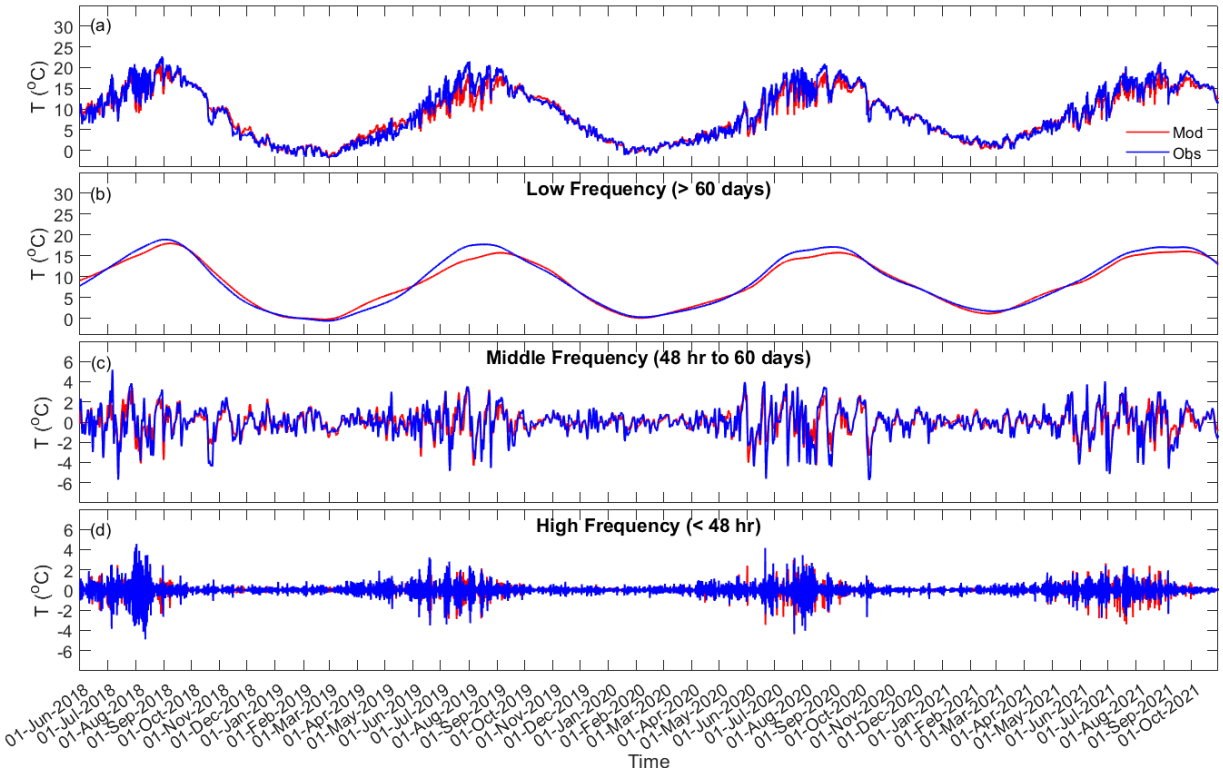

Fig. 4 Taylor Head bottom water temperature time series (a), and time series of the bottom water temperature in low (> 60 days (seasonal band); b), middle (48 hr to 60 days (meteorological band); c), and high (< 48 hr; d) frequencies from observation data (blue) and model results (red).

357

Table 3 Summary statistics of the bottom water temperature for the period 01/06/2018 to 31/05/2021 from model results and observation data (bottom row for each site *in italics*) at each site including mean, maximum, and minimum temperatures, temperature variability (standard deviation (SD)), and the 95th percentile temperature.

Site	Mean Temp (°C)	SD Temp (°C)	SD Met. Band (°C)	SD High Freq. Band (°C)	Ratio SD High Freq :Met.	Max Temp (°C)	Min Temp (°C)	95th percentile Temp (°C)
Port l'Hebert	11.62	8.75	2.14	1.03	0.48	30.52	-4	24.96
	10.93	*7.86*	*1.77*	*0.88*	*0.49*	*28.81*	*-3.97*	*22.99*
Port Joli	11.44	8.40	1.93	1.05	0.54	29.77	-4	24.37
	11.18	*7.79*	*1.77*	*1.07*	*0.60*	*29.57*	*-3.89*	*23.36*
Mason's Island	8.30	5.25	0.62	0.56	0.89	18.79	-1.81	15.50
	9.14	*6.34*	*0.79*	*0.58*	*0.73*	*21.61*	*-1.68*	*18.48*
Sacrifice Island	8.01	4.76	0.60	0.36	0.60	18.20	-1.44	16.15
	9.28	*5.87*	*0.90*	*0.41*	*0.46*	*21.96*	*-1.14*	*18.36*
Sambro	7.37	4.05	1.02	0.43	0.42	18.90	0.03	15.06
	6.84	*5.85*	*1.70*	*0.32*	*0.21*	*20.89*	*-1.25*	*17.82*
Taylor Head	7.89	5.63	1.09	0.41	0.38	20.70	-1.92	16.70
	8.10	*6.21*	*1.33*	*0.54*	*0.40*	*22.76*	*-1.71*	*18.83*

Table 4 Summary statistics of the bottom water temperature from model results and observation data (bottom row for each site *in italics*) during the summer growing periods (time series of 4 summer periods of June 1-Sept 15 between 01/06/2018 and 31/05/2021) at each site including mean, maximum, and minimum temperatures, temperature variability (standard deviation (SD)), and the 95th percentile temperature.

Site	Mean Temp (°C)	SD Temp (°C)	SD Met. Band (°C)	SD High Freq. Band (°C)	Ratio SD High Freq :Met.	Max Temp (°C)	Min Temp (°C)	95th percentile Temp (°C)
Port l'Hebert	22.14	3.09	1.76	1.29	0.73	30.53	10.84	26.64
	19.92	*3.23*	*1.75*	*1.08*	*0.62*	*28.81*	*9.10*	*24.67*
Port Joli	21.57	3.07	1.83	1.29	0.70	29.77	10.66	25.95
	20.15	*3.24*	*1.78*	*1.30*	*0.72*	*29.57*	*8.66*	*24.99*
Mason's Island	13.64	1.83	0.62	0.88	1.42	18.59	8.07	16.58
	16.09	*2.62*	*0.95*	*0.79*	*0.93*	*21.61*	*7.75*	*19.65*
Sacrifice Island	12.43	1.89	0.80	0.46	0.57	18.03	6.95	15.65
	15.29	*2.98*	*1.28*	*0.58*	*0.45*	*21.96*	*6.50*	*19.46*
Sambro	9.19	3.06	1.58	0.67	0.42	18.00	2.44	14.77
	12.25	*3.89*	*2.30*	*0.48*	*0.21*	*20.89*	*4.25*	*18.87*
Taylor Head	12.70	3.29	1.59	0.68	0.43	20.17	3.11	17.57
	14.64	*3.08*	*1.92*	*0.83*	*0.43*	*22.77*	*3.97*	*20.02*

3.3 Spectral analysis

Spectral analysis of the bottom water temperature shows that the model can reproduce the dominant water temperature variations found in each observed time series from the eelgrass sites (Fig. 5). Dominant frequencies are associated with the meteorological band (>48 hr) followed by diurnal variations, which also includes diurnal tides as well as temperature variation from solar heating, and finally semi-diurnal tides (~12 h). The presence of these frequencies at all sites in the power spectra of bottom water temperature indicates the strong effect of these processes on temperature dynamics. From the power spectra, the influence of solar and tidal heating at the shallower sites (i.e., Port l'Hebert (Fig. 5a), Port Joli (Fig. 5b), and Mason's Island (Fig. 5c) with mean depth at high tide < 2 m; Table 1) was greater than the other sites (i.e., Sacrifice Island (Fig. 5d), Sambro (Fig. 5e), and Taylor Head (Fig. 5f), mean depth at high tide >3m; Table 1).

Peaks at frequencies associated with overtides (periods of 3-10 hr) were evident at most sites (we note the model underestimation in most sites). The most significant overtides occurred at Port l'Hebert, Port Joli, and Mason's Island due to the relatively strong bottom friction, while overtides were less evident in the temperature spectrum of Sacrifice Island, and were negligible in Taylor Head and Sambro, the deepest sites.

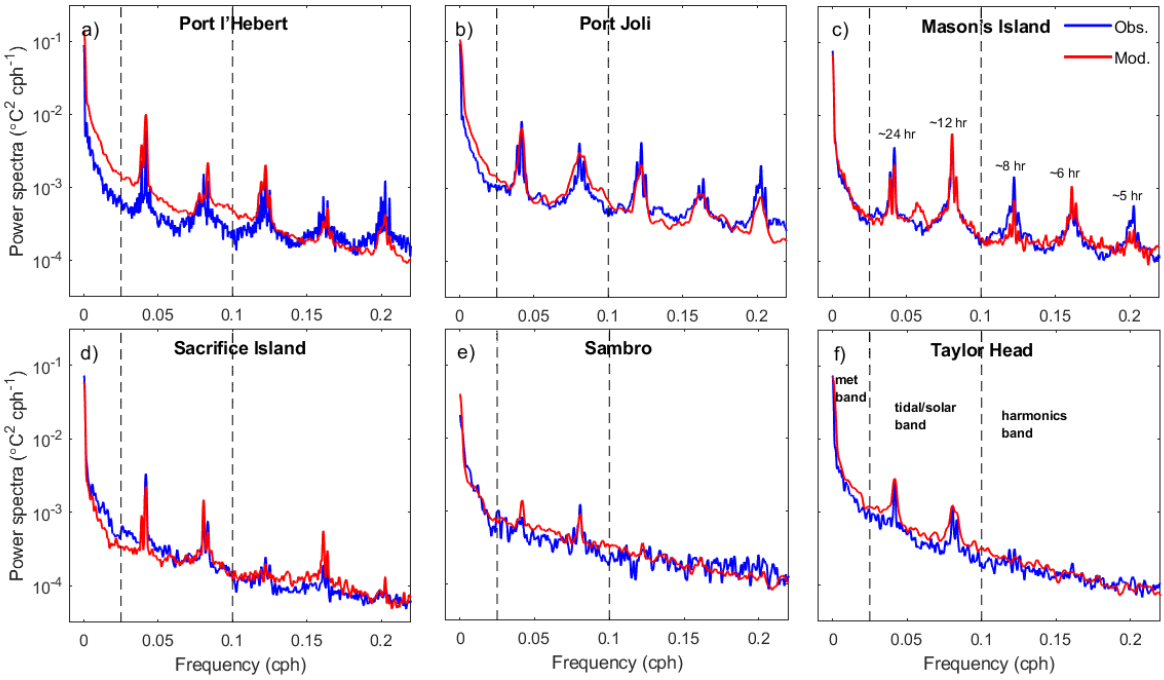

Fig. 5 Power spectra of bottom water temperature from observed data (blue) and model results (red) at Port l'Hebert (a), Port Joli (b), Mason's Island (c), Sacrifice Island (d), Sambro (e), and Taylor Head (f). Dashed lines show the limits of the low, middle, and high frequency bands considered (see panel f). The periods associated with the peaks in frequencies are shown in panel c.

3.4 Eelgrass specific temperature metrics

3.4.1 Summary statistics for the growing season

To highlight the differences among sites for eelgrass growth, summary statistics in the summer growing period were calculated. These metrics were averaged over 4 summer periods (June 1-Sept 15) between 01/06/2018 and 31/05/2021) (Table 4). From the model calculations, the warmest temperatures were at Port l'Hebert and Port Joli (22.14 °C and 21.57 °C, respectively) and the coldest temperatures at Sambro (9.19°C), while intermediate temperatures were found at Mason's Island, Sacrifice Island, and Taylor Head (13.64 °C, 12.43°C, and 12.70 °C, respectively). Model calculations and observed data also show the highest maximum temperature and 95th percentile temperature at Port l'Hebert and Port Joli, but the lowest minimum temperature in Sambro and Taylor Head. Generally, the model calculation of the summary statistics during the summer growing period are within 2 °C of the observed data (Table 4).

3.4.2 Growing degree day (GDD)

Figure 6 shows plots GDD during 01 June 2018 to 25 April 2019 at all sites (Table 1). The discrepancies between the GDD from the model predictions and those from the observations are < 15% (Figs. 4a-5a and S2a-S5a) and strongly influenced by the bias in the mean temperature between model and observations in the bottom water time series. The largest discrepancies were observed for Mason's Island and Sacrifice Island. Heat accumulation varies across the sites, with heat accumulating earliest and fastest at Port l'Hebert and Port Joli, at intermediate levels for Mason's Island, Sacrifice Island, and Taylor Head, and being latest and slowest at Sambro. Maximum heat accumulation was highest at Port l'Hebert and Port Joli, and lowest at Sambro. Heat accumulation was associated with depth, with heat accumulation reaching highest maximums and having highest rates of accumulation (i.e., initial slope in GDD) at shallow sites (Port l'Hebert, Port Joli) as compared to deeper sites. Accumulation of heat happened in the spring, summer, and fall from both model and observed data with negligible accumulation in

winter, starting in December, when the temperature dropped below the set threshold of 5°C used in the GDD calculation (Eq. 2) (Figure 6).

3.4.3 Warm water events

Warm water events, where the bottom water temperature is > 20°C, 23°C, or 27°C for > 2 hr and each event is separated by > 3 days, is calculated from 10/06/2018 to 31/05/2021 (Figure 7). This period covers three summer seasons with the observed data available from all sites except for summer 2019 in Sambro, where the warm events are less likely due to the large depth (Krumhansl et al., 2020; Wong and Dowd, 2021). From the observations and the model results, the warm water events only occurred at Port Joli and Port l'Hebert based on both the 23°C and 27°C criteria (Fig.7 b, c, e, and f), while other sites also experience warm events based on 20°C criteria (Fig. 7a and d). Based on 23°C, an average of 15.3 events $year^{-1}$ in Port Joli (from observations and model), and 16.3 and 11.3 events $year^{-1}$ from model and observations, respectively, in Port l'Hebert (Fig. 7b) were evident. These events occurred during June to September (Figs. 4a and S2a) with an average duration of 12.7 and 6.78 hr per event from model and observations, respectively, in Port Joli and 16.9 and 10.7 hr per event from model and observations, respectively, in Port l'Hebert. It is notable that the calculated numbers of warm events were highly dependent on the definition of these events (e.g., duration, length, and separation of events) due to high temporal variations of temperature. That is, a small change in the definition could result in quite different values, e.g. based on a 27 °C threshold from the model results, an average of 3 events $year^{-1}$ with an average duration of 3.7 hr occurred in Port Joli, and an average of 5.3 events $year^{-1}$ with an average duration of 5.5 hr occurred in Port l'Hebert. The duration and number of events based on 20 °C criteria were much higher than those based on 23 °C and 27 °C. Specifically, short durations of warm events (≤ 3 hr) based on

20 °C are observed in the sites that are deeper than Port l'Hebert and Port Joli (the model did not predict warm events in Mason's Island, Sacrifice Island, and Sambro). The discrepancies in the mean duration of events between the model results and those from the observed data were generally within the standard deviation of calculations (Fig. 7d, e, and f).

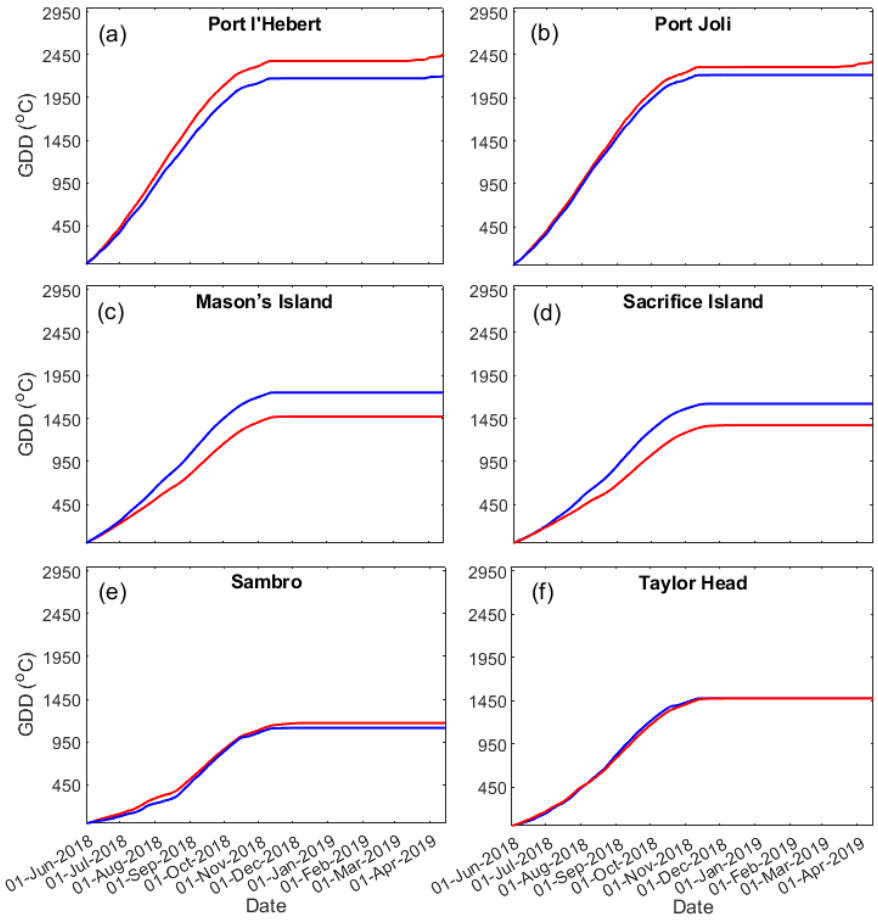

Fig. 6 Growing degree days at Port l'Hebert (a), Port Joli (b), Mason's Island (c), Sacrifice Island (d), Sambro (e), and Taylor Head (f) from the model (red) and observations (blue) for the growing season period 01/06/2018 to 25/04/2019.

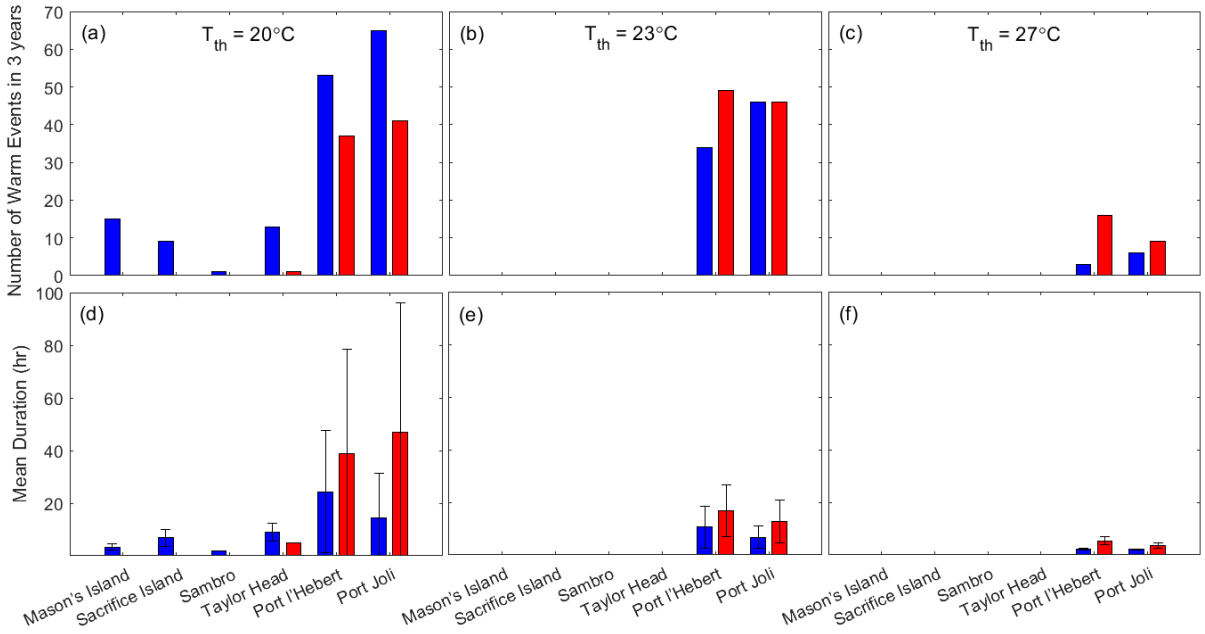

Fig. 7 Number (a, b, c) and duration (d, e, f) of warm events (for ≥ 2 hr; distinct events are separated by ≥ 3 days) when the bottom water temperature is greater than the threshold temperature (T_{th}) of 20°C (a and d), 23°C (b and e) and 27°C (c and f) for the growing seasonal period 10/06/2018 to 31/05/2021 from the model (red) and observations (blue). The length of the error bars in d, e, and f correspond to the standard deviations.

3.4.4 Daily temperature variabilities

Figure 8 compares the daily bottom water temperature range and its probability density estimate (via kernel density estimation) for the eelgrass sites. Shallow sites in general experienced higher daily temperature variations with lower peak probability and greater spread than the deeper sites, e.g., maximum monthly average of daily range in Port l'Hebert (Fig. 8a) and Port Joli (Fig. 8c) was 5 °C, compared to < 3 °C in Sambro (Fig. 8i) and Taylor Head (Fig. 8k). A daily temperature range of > 10 °C also occurred occasionally in Port l'Hebert and Port Joli. While the daily variations show a seasonal trend across all sites, with increased values during the warm seasons (June-September), shallower sites can experience daily variations > 5 °C during the winter seasons. Daily temperature variations can be due to daily solar heating and cooling and

tidal advection (Krumhansl et al., 2020), as well as occasional wind driven changes that can amplify water temperature changes.

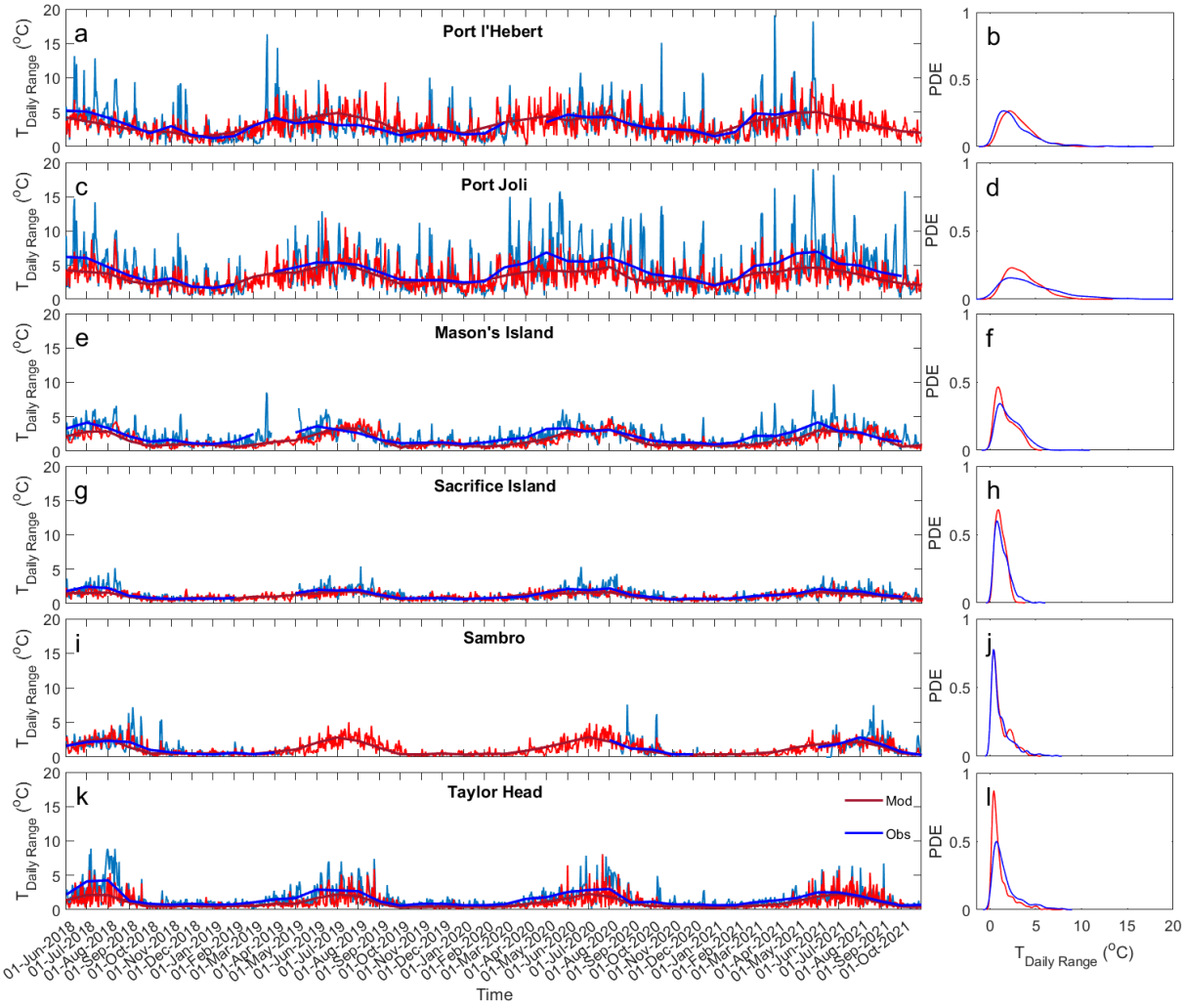

Fig. 8 Time series (a, c, e, g, I, k) and probability density estimate (PDE; b, d, f, h, j, l) of daily bottom water temperature range at Port l'Hebert (a and b), Port Joli (c and d), Mason's Island (e and f), Sacrifice Island (g and h), Sambro (i and j), and Taylor Head (k and l) from observed data (light and dark blue showing daily and monthly average, respectively) and model results (light and dark red: daily and monthly average, respectively).

3.5 Heat balance

The heat balance during the three years from 2019 to 2021 was calculated using model results at Port l'Hebert and Taylor Head to illustrate the seasonal contribution of different factors to temperature changes at these two sites that contrast in both depth and exposure (daily-averaged values shown in Fig. 9 and note the scale difference in the y-axes between the two sites). While a seasonal variability is evident in the change in the heat content at both sites (δT^{Avg}; Figs. 9a and c), with the maximum values during the warm seasons (~June-September), δT^{Avg} values at Port l'Hebert are greater than those at Taylor Head. Specifically, δT^{Avg} at Taylor Head is negligible during colder seasons (~November-February) with maximum daily-averaged values less than 0.03 °C hr^{-1}. These observed variabilities in temperature change are consequence of the contributing factors to the overall heat content at each site (Eq. 3).

Heat flux through the surface (δT^{SHF}) shows a seasonal variability with higher values during the warm seasons (Figs. 9a and c) at both sites. Higher δT^{SHF} at Port l'Hebert compared to Taylor Head (e.g., maximum summer daily-averaged values of > 0.25 °C hr^{-1} vs < 0.1 °C hr^{-1}, respectively) could be due to the difference in the depth of the sites as the surface heat flux per unit area at these two sites are comparable (Fig. S6). Low values of δT^{SHF} in the winter at Taylor Head (maximum daily-averaged values < 0.05 °C hr^{-1}) indicates negligible contribution of surface heat flux in the cold seasons at this site. The advective flux at both sites (δT^{Adv}) (Figs. 9b and d) show also seasonal variations with peak values during warm seasons.

Figure 10 shows the monthly mean of each term in the heat budget at both sites computed from daily-averaged values for 3 years (2019-2021). The monthly temperature change (δT^{Avg}) was small, for any year, at the sites. In all years, the mean temperature change in the warmer months (<0.02°C hr^{-1}) was 1-2 orders of magnitude smaller than the contribution to the

470 temperature change from the mean surface heat flux (0.2 °C hr^{-1} and 0.05 °C hr^{-1}, at Port
471 l'Hebert and Taylor Head, respectively). Monthly mean contribution from advective fluxes in the
472 warm months appeared to anti-correlate with the incoming surface heat flux showing that these
473 processes largely compensate for each other at the study sites.

474 Monthly mean magnitude of each term in the heat budget show similar values during the
475 3 years of the calculation, which suggests little interannual variability at both sites (Fig. 10). The
476 monthly contribution of the residuals in the heat budget (Figs. 9c and d) was generally less than
477 the leading term at both sites throughout the 3 years (Fig. 10). The residuals could be due to
478 factors not represented well in the simple formulation used in this study (e.g., eddies or other
479 complex 3D processes; Eq. 3).

480

481

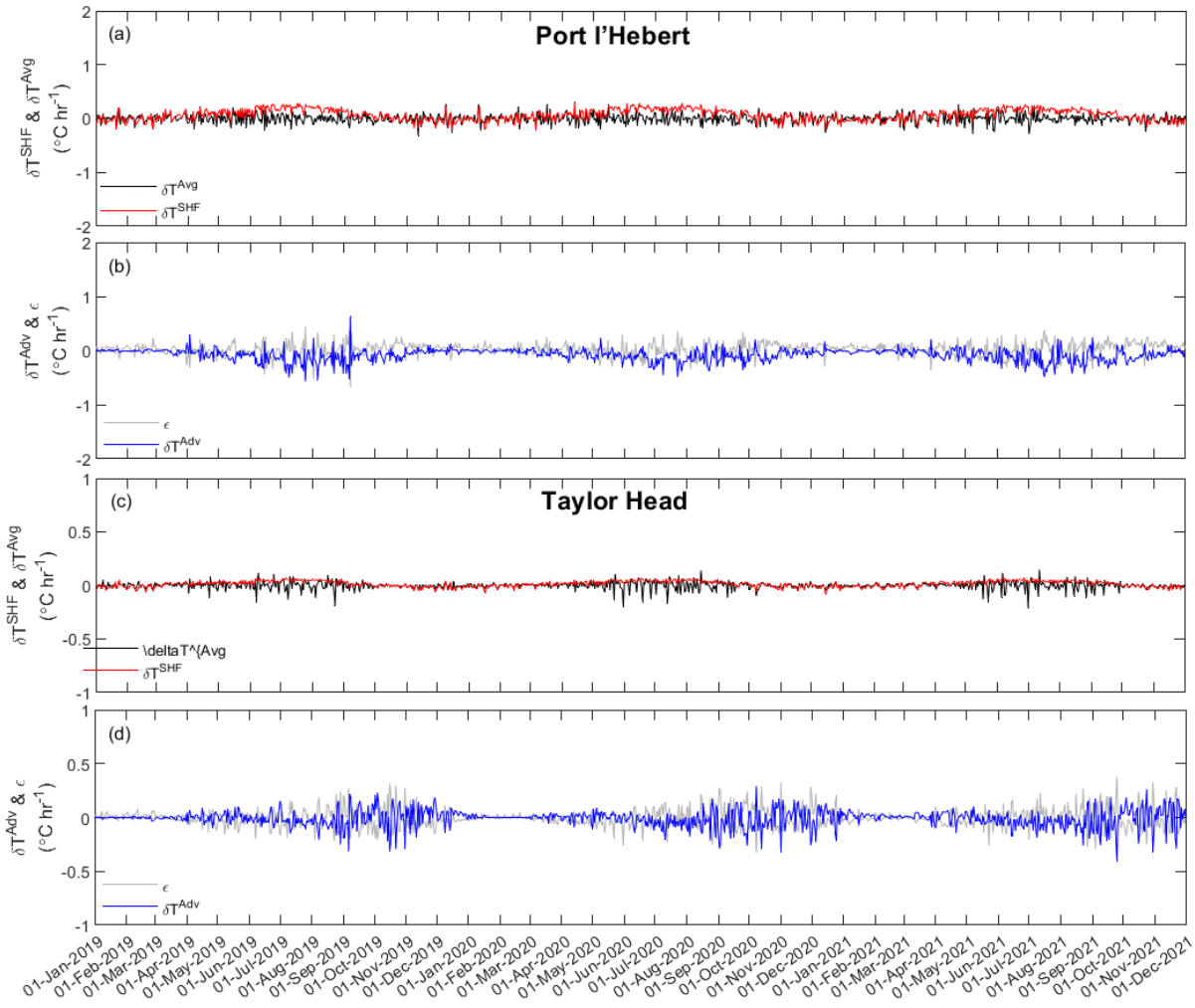

Fig. 9 Daily averaged temporal change in the heat content (δT^{Avg}; black), surface heat flux (δT^{SHF}; red), advective flux (δT^{Adv}; blue), and heat budget balance residual (ε; grey) at Port l'Hebert (a and b) and Taylor Head (c and d). Note the scale difference in the y-axes between the two sites.

482

483

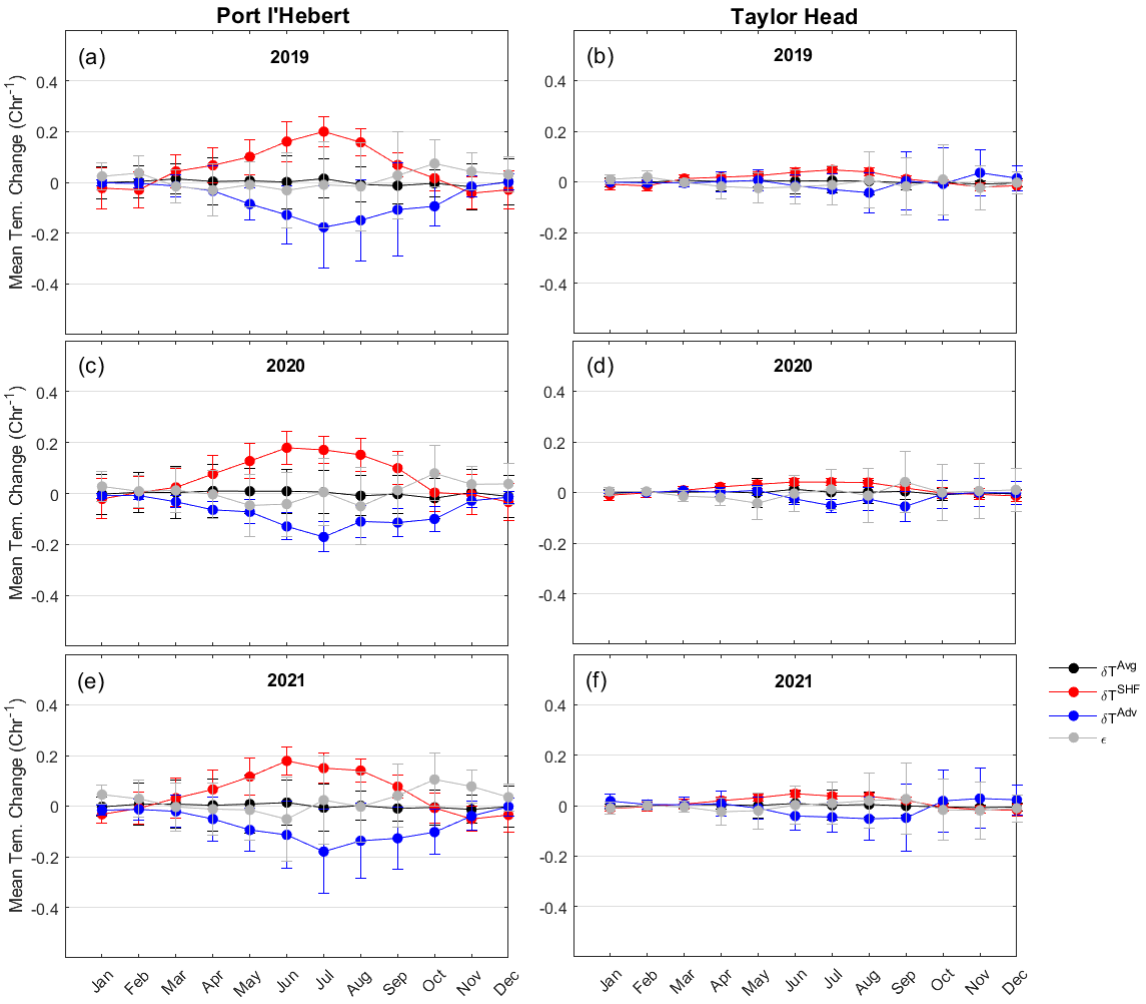

Fig. 10 Monthly mean of each term in heat budget (change in the heat content of the cross section (δT^{Avg}; black), surface heat flux (δT^{SHF}; red), advective flux (δT^{Adv}; blue), and heat budget balance residual (ε; grey) at Port l'Hebert (a, c, e) and Taylor Head (b, d, f) in 2019 (a and b), 2020 (c and d), and 2021 (e and f). The length of the error bars show the standard deviation.

4 Discussion and Conclusions

We investigated biologically relevant temperature dynamics in the nearshore regions of the Atlantic coast of Nova Scotia, illustrated at specific sites on time and space scales that are important for understanding eelgrass ecosystem functioning. Time series of water temperature from observations and FVCOM model results for June 2018 to May 2021 at six different

eelgrass sites showed that mean water temperatures during this period differed by > 4°C across the eelgrass beds with the maximum difference between the shallowest and the deepest of the sites (Port l'Hebert and Sambro, respectively; Table 3). This difference is > 7°C during summer growing period (Table 4). The two shallowest sites (Port l'Hebert, Port Joli) experienced several extreme warm events per year, while occurrence of these events was rare in the other sites. This indicates that eelgrasses inhabits a wide range of temperature regimes that have previously been shown to influence their performance. Most importantly, we have demonstrated that our numerical model can generally predict well the key attributes of temperature relevant to eelgrass ecosystems, and do so across large spatial scales, in this case the whole Atlantic coast of Nova Scotia. The resolutions allow for detailed site-specific temperature studies at different eelgrass beds, and the model can help identify at-risk areas resulting from temperature stress, now and in the future (Krumhansl et al., 2020; Wong and Dowd, 2021).

While an overall good agreement between the model predictions and the observed temperature was found, some discrepancies were evident. One important issue is that summer temperatures at the shallow sites (Port l'Hebert and Port Joli) were consistently overestimated, which should be considered when using the study results to assess ecological implications of various temperature processes (e.g., growing degree days is quite sensitive to this discrepancy). A potential reason could be the complex bathymetry of the tidal channels in the nearshore regions, which controls the heat exchanges between the inner region of the bays and the offshore waters. Firstly, model bathymetries in the tidal channels may be too shallow, which would significantly decrease the inward advection of cold offshore water and lead to overestimated water temperature in the inner bay. Secondly, the horizontal resolution of the air forcing (e.g., air-sea heat fluxes) from ERA5 is 31 km, which is relatively coarse compared to the model

513 resolution used in this study. Hence, some tidal channels (e.g., Port l'Hebert and Port Joli) are
514 represented as being on land in ERA5, which may cause artificially high water temperature in
515 summer. Thirdly, the overestimated water temperature in summer could also be caused by the
516 uncertainty in solar radiation attenuation properties in the bottom layer, where the solar radiation
517 not only heats the water, but also the bottom sediment due to the shallow water depth. Since the
518 amount of the solar energy stored in the sediment is unknown, we considered all the solar energy
519 as being distributed through the water column. To examine this process, we ran the model with
520 different water column attenuation coefficients for solar radiation and found that the model
521 performance can be improved by tuning them, however, development of a realistic attenuation
522 parameterization in the bottom layer is beyond the scope of the present paper. Generally,
523 however, the model simulated time series of the water temperature had a Willmott skill > 0.7,
524 and we were able to assess this in a frequency dependent manner. Summary statistics during the
525 summer growing period from the model were within 2°C from the recorded data in most sites
526 (Table 4). The discrepancies between growing degree day from the model calculation and the
527 observations (≤ 15%) were consistent with the systematic differences in the time series of bottom
528 water temperature. While the number and duration of warm events highly depended on the
529 definition used (e.g., duration, length, and separation of events) due to the high temporal
530 variation of temperature, the discrepancies in the mean duration of events between the model
531 results and those from the observed data were generally within the error standard deviation of
532 calculations.

533 Previous studies have suggested that short-term, sub-seasonal physical processes (i.e.,
534 warming events, wind events, upwelling) play an important role in eelgrass growth and
535 productivity (Wong et al. 2013, 2020, 2021; Krumhansl et al. 2021). While all sites experienced

a similar seasonal variation in the bottom water temperature, temperature variability on sub-seasonal scales was markedly different across the sites. Higher water temperature in the high frequency band (<48 hr; Table 3 and Figs. 4d-5d and S2d-S5d), larger dominance of solar heating and diurnal tides relative to the semi-diurnal tides (Fig. 2), and relatively higher daily temperature range (Figs. 8 and S6) indicate a greater impact of processes on time scales < 48 hr at shallow sites (Port l'Hebert, Port Joli, Mason's Island) compared to the other sites. Temperature variations in the meteorological band that were observed in all the sites (Figs. 4c-5c and S2c-S5c) can be due to local wind events as well as coast-wide processes such as storms and wind-driven coastal upwellings. A coastal upwelling index based on Ekman transport and upwelling favorable winds (Petrie et al., 1987) has shown strong coherence with the meteorological temperature band in eelgrass sites at the eastern Scotian Shelf (Krumhansl et al., 2021), which can transfer cool nutrient rich water to the surface and support eelgrass growth and photosynthesis during periods of nutrient limitation (Sandoval-Gil et al., 2019).

The simple heat balance analysis contrasting a shallow protected bay (Port l'Hebert) and a deeper exposed (Taylor Head) site showed that while the maximum annual changes in the heat content at the shallow site are greater than those at the deep site, the surface heat flux is the main contributor to the temperature variations during summer growing seasons at both sites (Fig. 10). Monthly mean contribution of the advective fluxes in both sites was negative and buffering the surface heating in the warm months. Monthly mean magnitude of the contributing terms in the heat budget showed small interannual variabilities at both sites.

Extended high temperature can have negative impacts on eelgrass health. Physiological impacts on eelgrass occur within 1-7 days when temperatures are 19-28°C (Evans et al., 1986, Gao et al., 2017), or as short as 15 min at > 30°C. Our results showed > 2 hr warm water events

occurred only at Port Joli and Port l'Hebert based on 23°C (optimum temperature for photosynthesis; > 12 events year^{-1}) and 27°C thresholds, while other sites experienced these events based on a 20°C criteria. In shallow sites, these events are likely due to long periods of solar heating over the extensive shallow flats (Wong et al., 2013). Warm water events based on the 23°C threshold typically lasted > 10 hr. The high frequency of warm events in the eelgrass sites in this study suggest that these eelgrass frequently experienced physiologically unfavorable conditions. Alternatively, anomalous warming can result in persistent changes in eelgrass bed characteristics across multiple clonal generations and years (DuBois et al., 2020). Previous studies show that these events are typical on the Atlantic coast of Nova Scotia (Wong et al., 2013, Wong 2018, Krumhansl et al., 2021), and that eelgrass can thermally adapt to varying temperature regimes, similar to other seagrass species (Marin-Guirao et al., 2016).

In summary, the FVCOM model developed for this study was able to reasonably predict water temperature variations and thermal metrics relevant to eelgrass condition. Eelgrass habitats occur in nearshore regions with localized and complex hydrodynamic regimes, and are also exposed to shelf scale wind driven events that control the water temperature (Feng et al., 2022; Wong and Dowd, 2021; Petrie et al., 1987). Representation of nearshore dynamics and its impact on coastal water temperature can only be achieved by predicting physical dynamics across large spatial scales by using targeted calibrated and validated high resolution numerical models. These can improve our general understanding of the interaction between the physical and biological processes in the coastal environments. It is hoped that results of this study, and the numerical model developed here, can contribute towards the conservation and protection of eelgrass beds, and the maintenance of their ecosystem functioning in this era of climate change.

582 **Acknowledgements**

583 We thank L Zhai, RHorwitz, and YMa at the Bedford Institute of Oceanography for insightful
584 reviews. M Dowd was supported by an NSERC Discovery grant.
585

586

References

Bakirman, T., Gumusay, M.U., 2020. A novel GIS-MCDA-based spatial habitat suitability model for Posidonia oceanica in the Mediterranean. Environ. Monit. Assess. 192. https://doi.org/10.1007/s10661-020-8198-1

Biebl, R., McRoy, C.P., Marsh, J.A., Dennison, W.C., Alberte, R.S., 1971. Effects of temperature on photosynthesis and respiration in eelgrass (Zostera marina L.). J. Exp. Mar. Bio. Ecol. 101, 257–267. https://doi.org/https://doi.org/10.1016/0022-0981(86)90267-4

Brander, K., Hurley, P.C.F., 1992. Distribution of early-stage Atlantic cod (Gadus morhua), haddock (Melanogrammus aeglefinus), and witch flounder (Glyptocephalus cynoglossus) eggs on the Scotian Shelf: a reappraisal of evidence on the coupling of cod spawning and plankton production. Can. J. Fish. Aquat. Sci. 49, 238–251. https://doi.org/10.1139/f92-028

Brickman, D., Hebert, D. and Wang, Z., 2018. Mechanism for the recent ocean warming events on the Scotian Shelf of eastern Canada. Continental Shelf Research, 156, pp.11-22.

Chen, C., Huang, H., Beardsley, R.C., Liu, H., Xu, Q., Cowles, G., 2007. A finite volume numerical approach for coastal ocean circulation studies: Comparisons with finite difference models. J. Geophys. Res. Ocean. 112. https://doi.org/https://doi.org/10.1029/2006JC003485

Chen, C., Liu, H., Beardsley, R.C., 2003. An Unstructured Grid, Finite-Volume, Three-Dimensional, Primitive Equations Ocean Model: Application to Coastal Ocean and Estuaries. J. Atmos. Ocean. Technol. 20, 159–186. https://doi.org/10.1175/1520-0426(2003)020<0159:AUGFVT>2.0.CO;2

Dever, E.P., Lentz, S.J., 1994. Heat and salt balances over the northern California shelf in winter and spring. J. Geophys. Res. Ocean. 99, 16001–16017. https://doi.org/https://doi.org/10.1029/94JC01228

Dever, M., Hebert, D., Greenan, B., Sheng, J., Smith, P., 2016. Hydrography and Coastal

611 Circulation along the Halifax Line and the Connections with the Gulf of St. Lawrence.
612 ATMOSPHERE-OCEAN 54, 199–217. https://doi.org/10.1080/07055900.2016.1189397
613 Drinkwater, K.F., 1996. Atmospheric and oceanic variability in the Northwest Atlantic during
614 the 1980s and early 1990s. Journal of Northwest Atlantic Fishery Science, 18.
615 DuBois, K., Williams, S. L., and Stachowicz, J. J. 2020. Previous exposure mediates the
616 response of eelgrass to future warming via clonal transgenerational plasticity. Ecology 101:
617 1-12.
618 Dunic, J.C., Brown, C.J., Connolly, R.M., Turschwell, M.P., Côté, I.M., 2021. Long-term
619 declines and recovery of meadow area across the world's seagrass bioregions. Glob. Chang.
620 Biol. 27, 4096–4109. https://doi.org/https://doi.org/10.1111/gcb.15684
621 Egbert, G.D., Bennett, A.F., Foreman, M.G.G., 1994. TOPEX/POSEIDON tides estimated using
622 a global inverse model. J. Geophys. Res. Ocean. 99, 24821–24852.
623 https://doi.org/https://doi.org/10.1029/94JC01894
624 Egbert, G.D., Erofeeva, S.Y., 2002. Efficient Inverse Modeling of Barotropic Ocean Tides. J.
625 Atmos. Ocean. Technol. 19, 183–204. https://doi.org/https://doi.org/10.1175/1520-
626 0426(2002)019<0183:EIMOBO>2.0.CO;2
627 Feng, T., Stanley, R.R.E., Wu, Y., Kenchington, E., Xu, J., Horne, E., 2022. A High-Resolution
628 3-D Circulation Model in a Complex Archipelago on the Coastal Scotian Shelf. J. Geophys.
629 Res. Ocean. 127, 1–23. https://doi.org/10.1029/2021JC017791
630 Fourqurean, J.W., Duarte, C.M., Kennedy, H., Marbà, N., Holmer, M., Mateo, M.A., Apostolaki,
631 E.T., Kendrick, G.A., Krause-Jensen, D., Mcglathery, K.J., Serrano, O., 2012. Seagrass
632 ecosystems as a globally significant carbon stock. https://doi.org/10.1038/NGEO1477
633 Gan, J., San Ho, H., Liang, L., 2013. Dynamics of Intensified Downwelling Circulation over a

Widened Shelf in the Northeastern South China Sea. J. Phys. Oceanogr. 43, 80–94. https://doi.org/10.1175/JPO-D-12-02.1

Han, G., Loder, J.W., 2003. Three-dimensional seasonal-mean circulation and hydrography on the eastern Scotian Shelf. J. Geophys. Res. 108. https://doi.org/10.1029/2002jc001463

Han, G., Loder, J.W., Smith, P.C., 1999. Seasonal-Mean Hydrography and Circulation in the Gulf of St. Lawrence and on the Eastern Scotian and Southern Newfoundland Shelves. J. Phys. Oceanogr. 29, 1279–1301. https://doi.org/10.1175/1520-0485(1999)029<1279:SMHACI>2.0.CO;2

Hannah, C.G., Loder, J.W., and Wright, D.G., 1996. Seasonal variation of the baroclinic circulation in the Scotia-Maine region. Buoyancy Effects on Coastal and Estuarine Dynamics. D. G. Aubrey and C. T. Friedrichs, Eds., American Geophysical Union, 7-29.

Hannah, C.G., Shore, J.A., Loder, J.W., 2001. Seasonal circulation on the Western and Central Scotian Shelf. J. Phys. Oceanogr. 31, 591–615. https://doi.org/10.1175/1520-0485(2001)031<0591:SCOTWA>2.0.CO;2

Hughes, T.P., Kerry, J.T., Álvarez-Noriega, M., Álvarez-Romero, J.G., Anderson, K.D., Baird, A.H., Babcock, R.C., Beger, M., Bellwood, D.R., Berkelmans, R., Bridge, T.C., Butler, I.R., Byrne, M., Cantin, N.E., Comeau, S., Connolly, S.R., Cumming, G.S., Dalton, S.J., Diaz-Pulido, G., Eakin, C.M., Figueira, W.F., Gilmour, J.P., Harrison, H.B., Heron, S.F., Hoey, A.S., Hobbs, J.P.A., Hoogenboom, M.O., Kennedy, E. V., Kuo, C.Y., Lough, J.M., Lowe, R.J., Liu, G., McCulloch, M.T., Malcolm, H.A., McWilliam, M.J., Pandolfi, J.M., Pears, R.J., Pratchett, M.S., Schoepf, V., Simpson, T., Skirving, W.J., Sommer, B., Torda, G., Wachenfeld, D.R., Willis, B.L., Wilson, S.K., 2017. Global warming and recurrent mass bleaching of corals. Nature 543, 373–377. https://doi.org/10.1038/nature21707

Jean-Michel, L., Eric, G., Romain, B.-B., Gilles, G., Angélique, M., Marie, D., Clément, B., Mathieu, H., Olivier, L.G., Charly, R., Tony, C., Charles-Emmanuel, T., Florent, G., Giovanni, R., Mounir, B., Yann, D., Pierre-Yves, L.T., 2021. The Copernicus Global 1/12° Oceanic and Sea Ice GLORYS12 Reanalysis. Front. Earth Sci.

Katavouta, A., Thompson, K.R., Lu, Y. and Loder, J.W., 2016. Interaction between the tidal and seasonal variability of the Gulf of Maine and Scotian shelf region. Journal of Physical Oceanography, 46(11), pp.3279-3298.

Krumhansl, K.A., Dowd, M., Wong, M.C., 2021. Multiple Metrics of Temperature, Light, and Water Motion Drive Gradients in Eelgrass Productivity and Resilience. Front. Mar. Sci. 8, 597707. https://doi.org/10.3389/fmars.2021.597707

Krumhansl, K.A., Dowd, M., Wong, M.C., 2020. A characterization of the physical environment at eelgrass (Zostera marina) sites along the Atlantic coast of Nova Scotia Maritimes Region , Fisheries and Oceans Canada Canadian Technical Report of Fisheries and Aquatic Sciences 3361.

Laurence, G.C., Rogers, C.A., 1976. Effects of temperature and salinity on comparative embryo development and mortality of Atlantic cod (Gadus morhua L.) and haddock (Melanogrammus aeglefinus (L.)). ICES J. Mar. Sci. 36, 220–228. https://doi.org/10.1093/icesjms/36.3.220

Lee, K.-S., Park, S.R., Kim, Y.K., 2007. Effects of irradiance, temperature, and nutrients on growth dynamics of seagrasses: A review. J. Exp. Mar. Bio. Ecol. 350, 144–175. https://doi.org/https://doi.org/10.1016/j.jembe.2007.06.016

Lemagie, E., Kirincich, A., Lentz, S., 2021. The Summer Heat Balance of the Oregon Inner Shelf Over Two Decades: Mean and Interannual Variability. J. Geophys. Res. Ocean. 126,

1–18. https://doi.org/10.1029/2019JC015856

Lemagie, E., Kirincich, A., Lentz, S., 2020. The Summer Heat Balance of the Oregon Inner Shelf Over Two Decades: Mean and Interannual Variability. J. Geophys. Res. Ocean. 125, 1–18. https://doi.org/10.1029/2019JC015856

Liao, E., Oey, L.Y., Yan, X.-H., Li, L., Jiang, Y., 2018. The Deflection of the China Coastal Current over the Taiwan Bank in Winter. J. Phys. Oceanogr. 48, 1433–1450. https://doi.org/10.1175/JPO-D-17-0037.1

Liu, Y., MacCready, P., Hickey, B.M., Dever, E.P., Kosro, P.M., Banas, N.S., 2009. Evaluation of a coastal ocean circulation model for the Columbia river plume in summer 2004. J. Geophys. Res. Ocean. 114, 1–23. https://doi.org/10.1029/2008JC004929

Loder, J.W., Petrie, B.D., Gawarkiewicz, G., 1998. The coastal ocean off northeastern North America: A large-scale view. sea 11, 105–138.

Lotze, H.K., Lenihan, H.S., Bourque, B.J., Bradbury, R.H., Cooke, R.G., Kay, M.C., Kidwell, S.M., Kirby, M.X., Peterson, C.H., Jackson, J.B.C., 2006. Depletion degradation, and recovery potential of estuaries and coastal seas. Science (80-.). 312, 1806–1809. https://doi.org/10.1126/SCIENCE.1128035

Lynge, B.K., Berntsen, J., Gjevik, B., 2010. Numerical studies of dispersion due to tidal flow through Moskstraumen, northern Norway. Ocean Dyn. 60, 907–920. https://doi.org/10.1007/s10236-010-0309-z

Marbà, N., and Duarte, C. M., 2010. Mediterranean warming triggers seagrass (Posidonia oceanica) shoot mortality. Glob. Change. Biol. 16, 2366–2375. doi:10.1111/j.1365-2486.2009.02130.x

Marsh, J.A., Dennison, W.C., Alberte, R.S., 1986. Effects of temperature on photosynthesis and

703 respiration in eelgrass (Zostera marina L.). J. Exp. Mar. Bio. Ecol. 101, 257–267.
704 https://doi.org/https://doi.org/10.1016/0022-0981(86)90267-4
705 Marin-Guirao, L., Ruiz, J. M., Dattolo, E., Garcia-Munoz, E., and Procaccini, G. 2016.
706 Physiological and molecular evidence of differential short-term heat tolerance in
707 Mediterranean seagrasses. Nat. Sci. Rep. 6: 28615.
708 McWilliams, J.C., 2016. Submesoscale currents in the ocean. Proc. R. Soc. A Math. Phys. Eng.
709 Sci. 472, 20160117. https://doi.org/10.1098/rspa.2016.0117
710 Mills, K.E., Pershing, A.J., Brown, C.J., Chen, Y., Chiand, F.-S., Holland, D.S., Lehuta, S., Nye,
711 J.A., Sun, J.C., Thomas, A.C., Wahle, R.A., 2013. Fisheries management in a changing
712 climate: lessons from the 2012 ocean heat wave in the Northwest Atlantic. Oceanography
713 26, 191–195.
714 Moore, K. A., Shields, E. C., and Parrish, D. B., 2014. Impacts of varying estuarine temperature
715 and light conditions on zostera marina (Eelgrass) and its InteractionsWith Ruppia maritima
716 (Widgeongrass). Estuaries Coasts 37, 20–30. doi: 10.1007/s12237-013-9667-3
717 Murphy, G.E.P., Wong, M.C., Lotze, H.K., 2019. A human impact metric for coastal ecosystems
718 with application to seagrass beds in Atlantic Canada. FACETS 4, 210–237.
719 https://doi.org/10.1139/facets-2018-0044
720 Neuheimer, A.B., Taggart, C.T., 2007. The growing degree-day and fish size-at-age: The
721 overlooked metric. Can. J. Fish. Aquat. Sci. 64, 375–385. https://doi.org/10.1139/F07-003
722 Mtwana Nordlund, L., Koch, E. W., Barbier, E. B., & Creed, J. C. (2016). Seagrass ecosystem services
723 and their variability across genera and geographical regions. *Plos one*, *11*(10), e0163091.
724 Oliver, E.C.J., Donat, M.G., Burrows, M.T., Moore, P.J., Smale, D.A., Alexander, L. V,
725 Benthuysen, J.A., Feng, M., Sen Gupta, A., Hobday, A.J., Holbrook, N.J., Perkins-
726 Kirkpatrick, S.E., Scannell, H.A., Straub, S.C., Wernberg, T., 2018. Longer and more

727 frequent marine heatwaves over the past century. Nat. Commun. 9, 1324.
728 https://doi.org/10.1038/s41467-018-03732-9
729 Pawlowicz, R., Beardsley, B., Lentz, S., 2002. Classical tidal harmonic analysis including error
730 estimates in MATLAB using T_TIDE. Comput. Geosci. 28, 929–937.
731 https://doi.org/https://doi.org/10.1016/S0098-3004(02)00013-4
732 Petrie, B., 2007. Does the North Atlantic Oscillation affect hydrographic properties on the
733 Canadian Atlantic continental shelf?. Atmosphere-ocean, 45(3), pp.141-151.
734 Petrie, B., 1975. M2 surface and internal tides on the Scotian Shelf and Slope. J. Mar. Res. 33,
735 303–323.
736 Petrie, B., Drinkwater, K., 1993. Temperature and salinity variability on the Scotian Shelf and in
737 the Gulf of Maine 1945–1990. J. Geophys. Res. Ocean. 98, 20079–20089.
738 https://doi.org/https://doi.org/10.1029/93JC02191
739 Petrie, B., Topliss, B.J., Wright, D.G., 1987. Coastal upwelling and eddy development off Nova
740 Scotia. J. Geophys. Res. Ocean. 92, 12979–12991.
741 https://doi.org/https://doi.org/10.1029/JC092iC12p12979
742 Poje, A.C., Haza, A.C., Özgökmen, T.M., Magaldi, M.G., Garraffo, Z.D., 2010. Resolution
743 dependent relative dispersion statistics in a hierarchy of ocean models. Ocean Model. 31,
744 36–50. https://doi.org/https://doi.org/10.1016/j.ocemod.2009.09.002
745 Saava, I., Bennett, S., Roca, G., Jorda, G., and Marba, N., 2018. Thermal tolerance of
746 Mediterranean marine macrophytes: vulnerability to global warming. Ecol. Evol. 8, 12032–
747 12043. doi: 10.1002/ece3.4663
748 Sandoval-Gil, J.M., del Carmen Ávila-López, M., Camacho-Ibar, V.F., Hernández-Ayón, J.M.,
749 Zertuche-González, J.A., Cabello-Pasini, A., 2019. Regulation of Nitrate Uptake by the

Seagrass Zostera marina During Upwelling. Estuaries and Coasts 42, 731–742. https://doi.org/10.1007/s12237-019-00523-3

Sheng, J., Zhai, X. and Greatbatch, R.J., 2006. Numerical study of the storm-induced circulation on the Scotian Shelf during Hurricane Juan using a nested-grid ocean model. Progress in Oceanography, 70(2-4), pp.233-254.

Smith, P.C., Petrie, B., Mann, C.R., 1978. Circulation, Variability, and Dynamics of the Scotian Shelf and Slope. J. Fish. Res. Board Canada 35, 1067–1083. https://doi.org/10.1139/f78-170

Smith, P.C., Schwing, F.B., 1991. Mean circulation and variability on the eastern Canadian continental shelf. Cont. Shelf Res. 11, 977–1012. https://doi.org/10.1016/0278-4343(91)90088-N

Staehr, P.A., Borum, J., 2011. Seasonal acclimation in metabolism reduces light requirements of eelgrass (Zostera marina). J. Exp. Mar. Bio. Ecol. 407, 139–146. https://doi.org/https://doi.org/10.1016/j.jembe.2011.05.031

Strydom, S., Murray, K., Wilson, S., Huntley, B., Rule, M., Heithaus, M., et al., 2020. Too hot to handle: unprecedented seagrass death driven by marine heatwave in a World Heritage Area. Glob. Change. Biol. 26, 3525–3538. doi:10.1111/gcb.15065

Sutcliffe, W.H.Jr., R.H. Loucks, and K.F. Drinkwater (1976) Coastal circulation and physical oceanography of the Scotian Shelf and the Gulf of Maine. J. Fish. Res. Board Can. 33: 98-115.

Thompson, K.R., Loucks, R.H. and Trites, R.W., 1988. Sea surface temperature variability in the shelf-slope region of the Northwest Atlantic. Atmosphere-Ocean, 26(2), pp.282-299.

Umlauf, L., Burchard, H., 2005. Second-order turbulence closure models for geophysical boundary layers. A review of recent work. Cont. Shelf Res. 25, 795–827.

https://doi.org/https://doi.org/10.1016/j.csr.2004.08.004

Umoh, J.U. and Thompson, K.R., 1994. Surface heat flux, horizontal advection, and the seasonal evolution of water temperature on the Scotian Shelf. Journal of Geophysical Research: Oceans, 99(C10), pp.20403-20416.

Warner, J.C., Geyer, W.R., Lerczak, J.A., 2005. Numerical modeling of an estuary: A comprehensive skill assessment. J. Geophys. Res. Ocean. 110. https://doi.org/https://doi.org/10.1029/2004JC002691

Waycott, M., Duarte, C.M., Carruthers, T.J.B., Orth, R.J., Dennison, W.C., Olyarnik, S., Calladine, A., Fourqurean, J.W., Heck, K.L., Hughes, A.R., Kendrick, G.A., Kenworthy, W.J., Short, F.T., Williams, S.L., 2009. Accelerating loss of seagrasses across the globe threatens coastal ecosystems. Proc. Natl. Acad. Sci. U. S. A. 106, 12377–12381. https://doi.org/10.1073/pnas.0905620106

Wernberg, T., Bennett, S., Babcock, R.C., Bettignies, T. De, Cure, K., Depczynski, M., Dufois, F., Fromont, J., Fulton, C.J., Hovey, R.K., Harvey, E.S., Holmes, T.H., Kendrick, G. a, Radford, B., Santana-garcon, J., Saunders, B.J., Smale, D. a, Thomsen, M.S., Tuckett, C. a, Tuya, F., 2015. Temperate Marine Ecosystem. Science (80-.). 353, 169–172. https://doi.org/10.1126/science.aad8745

Wiberg, P. L., 2023. Temperature amplification and marine heatwave alteration in shallow coastal bays. Frontiers in Marine Science, 10, 1129295. https://doi.org/10.3389/fmars.2023.1129295

Wilkin, J.L., 2006. The Summertime Heat Budget and Circulation of Southeast New England Shelf Waters. J. Phys. Oceanogr. 36, 1997–2011. https://doi.org/10.1175/JPO2968.1

Willmott, C.J., 1981. ON THE VALIDATION OF MODELS. Phys. Geogr. 2, 184–194.

https://doi.org/10.1080/02723646.1981.10642213

Wong, M.C., 2018. Secondary Production of Macrobenthic Communities in Seagrass (Zostera marina, Eelgrass) Beds and Bare Soft Sediments Across Differing Environmental Conditions in Atlantic Canada. Estuaries and Coasts 41, 536–548. https://doi.org/10.1007/s12237-017-0286-2

Wong, M.C., Bravo, M.A., Dowd, M., 2013. Ecological dynamics of Zostera marina (eelgrass) in three adjacent bays in Atlantic Canada. Bot. Mar. 56, 413–424. https://doi.org/10.1515/bot-2013-0068

Wong, M.C., Dowd, M., 2021. Sub-seasonal physical dynamics of temperature, light, turbidity, and water motion in eelgrass (Zostera marina) beds on the Atlantic coast of Nova Scotia, Canada, Canadian Technical Report of Fisheries and Aquatic Sciences.

Wong, M.C., Dowd, M., 2023. The Role of Short-Term Temperature Variability and Light in Shaping the Phenology and Characteristics of Seagrass Beds. Ecosphere 14(11): e4698. https://doi.org/10.1002/ecs2.4698

Wong, M.C., Griffiths, G., Vercaemer, B., 2020. Seasonal Response and Recovery of Eelgrass (Zostera marina) to Short-Term Reductions in Light Availability. Estuaries and Coasts 43, 120–134. https://doi.org/10.1007/s12237-019-00664-5

Wong, M.C., Vercaemer, B.M., Griffiths, G., 2021. Response and Recovery of Eelgrass (Zostera marina) to Chronic and Episodic Light Disturbance. Estuaries and Coasts 44, 312–324. https://doi.org/10.1007/s12237-020-00803-3

Wu, Y., Chaffey, J., Greenberg, D.A., Colbo, K., Smith, P.C., 2011. Tidally-induced sediment transport patterns in the upper Bay of Fundy: A numerical study. Cont. Shelf Res. 31, 2041–2053. https://doi.org/10.1016/j.csr.2011.10.009

Wu, Y., Chaffey, J., Law, B., Greenberg, D.A., Drozdowski, A., Page, F., Haigh, S., 2014. A three-dimensional hydrodynamic model for aquaculture: A case study in the Bay of Fundy. Aquac. Environ. Interact. 5, 235–248. https://doi.org/10.3354/aei00108

Wu, Y., Hannah, C.G., O'Flaherty-Sproul, M., Thupaki, P., 2017. Representing kelp forests in a tidal circulation model. J. Mar. Syst. 169, 73–86. https://doi.org/10.1016/j.jmarsys.2016.12.007

Wu, Y., Sheng, J., Senciall, D. and Tang, C., 2016. A comparative study of satellite-based operational analyses and ship-based in-situ observations of sea surface temperatures over the eastern Canadian shelf. Satellite Oceanography and Meteorology, 1(1), pp.29-38.

Wu, Y., Tang, C., Hannah, C., 2012. The circulation of eastern Canadian seas. Prog. Oceanogr. 106, 28–48. https://doi.org/10.1016/j.pocean.2012.06.005

831

Supplementary Information

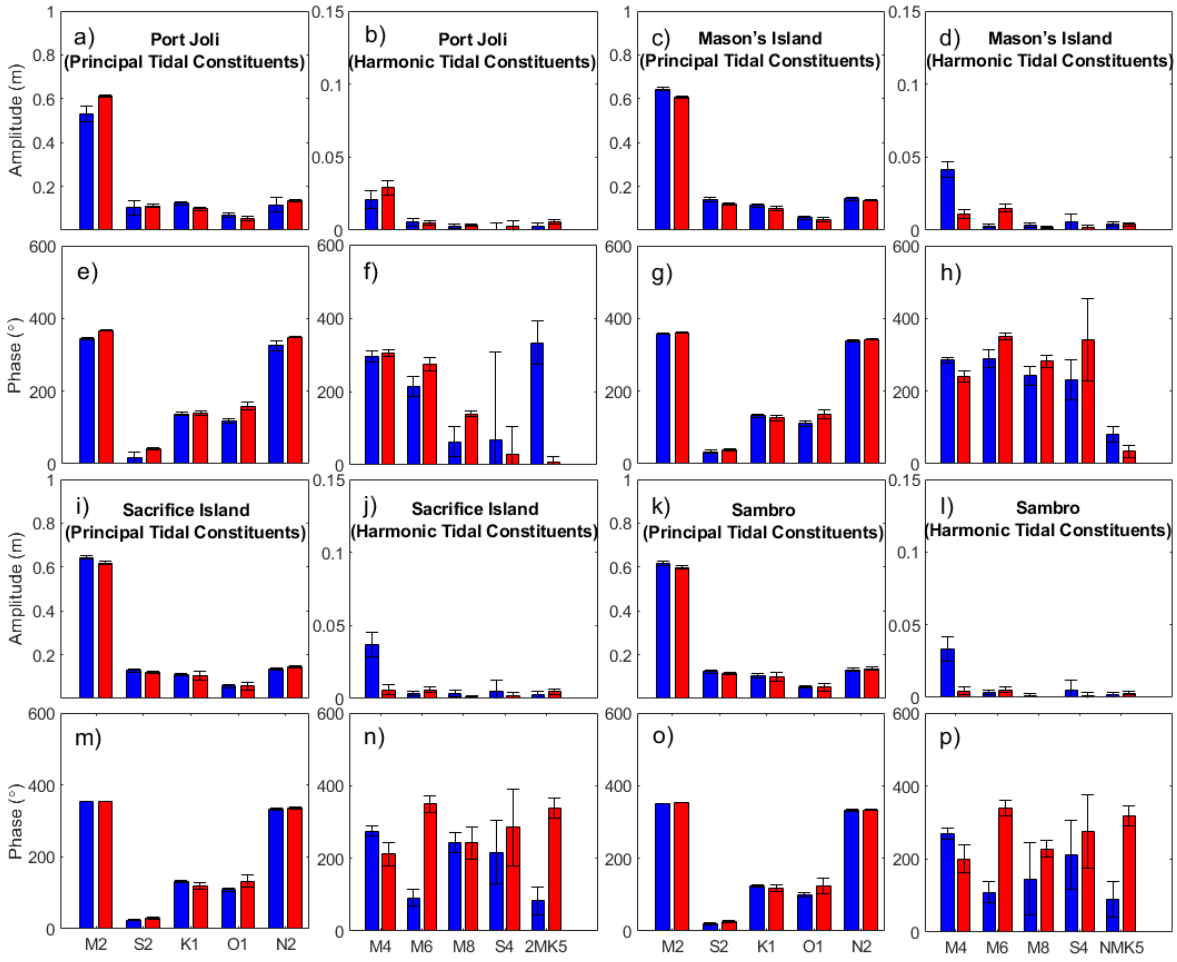

Fig. S1 Amplitude (1st and 3rd rows) and phase (2nd and 4th rows) of sea level for five select principal tidal constituents (M2, S2, K1, O1, and N2; panels a, i, m, c, g, k, and o) and five harmonic tidal components (M4, M6, M8, S4, and 2MK5; panels b, f, j, n, d, h, l, p) from observed data (blue) and model results (red) at Port Joli (a, b, e, and f), Mason's Island (c, d, g, and h), Sacrifice Island (i, j, m, and n), and Sambro (k, l, o, and p). Length of the error bars show the standard deviation.

832

833

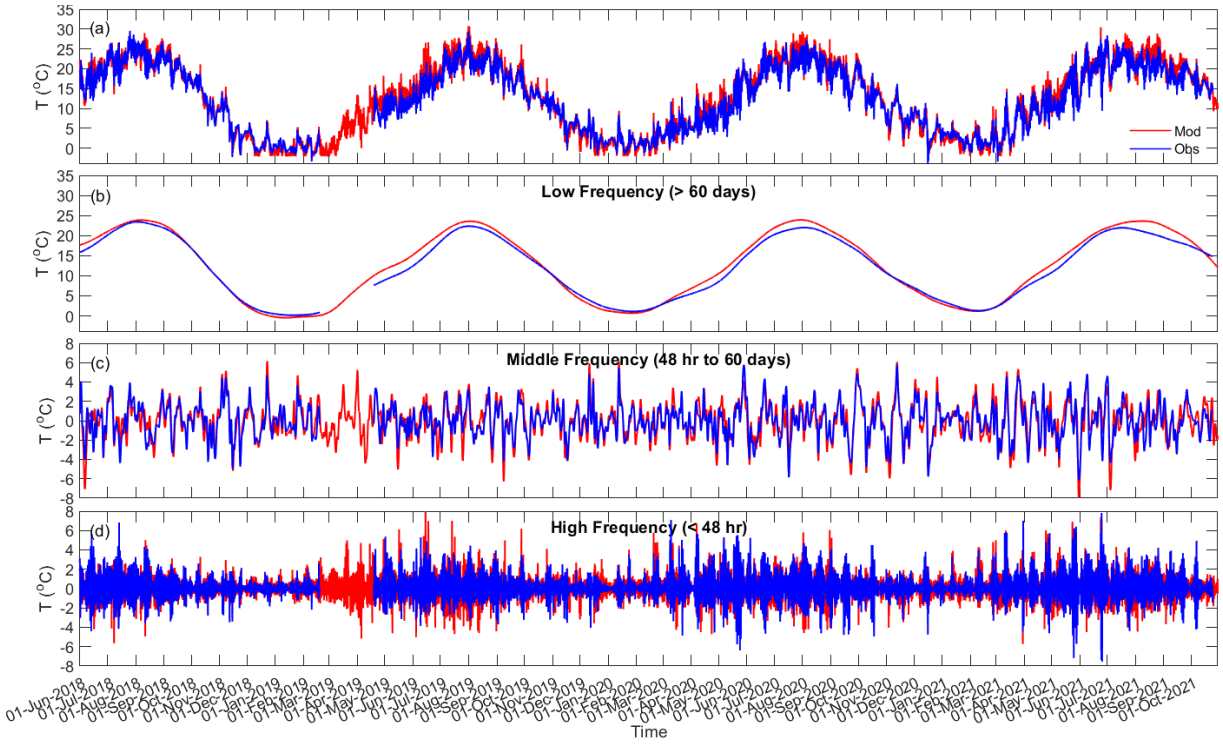

Fig. S2 At Port Joli, bottom water (~10 cm above the bed) temperature time series (a), and time series of the bottom water temperature in low (> 60 days (seasonal band); b), middle (48 hr to 60 days (meteorological band); c), and high (< 48 hr; d) frequencies from observation data (blue) and model results (red).

834

835

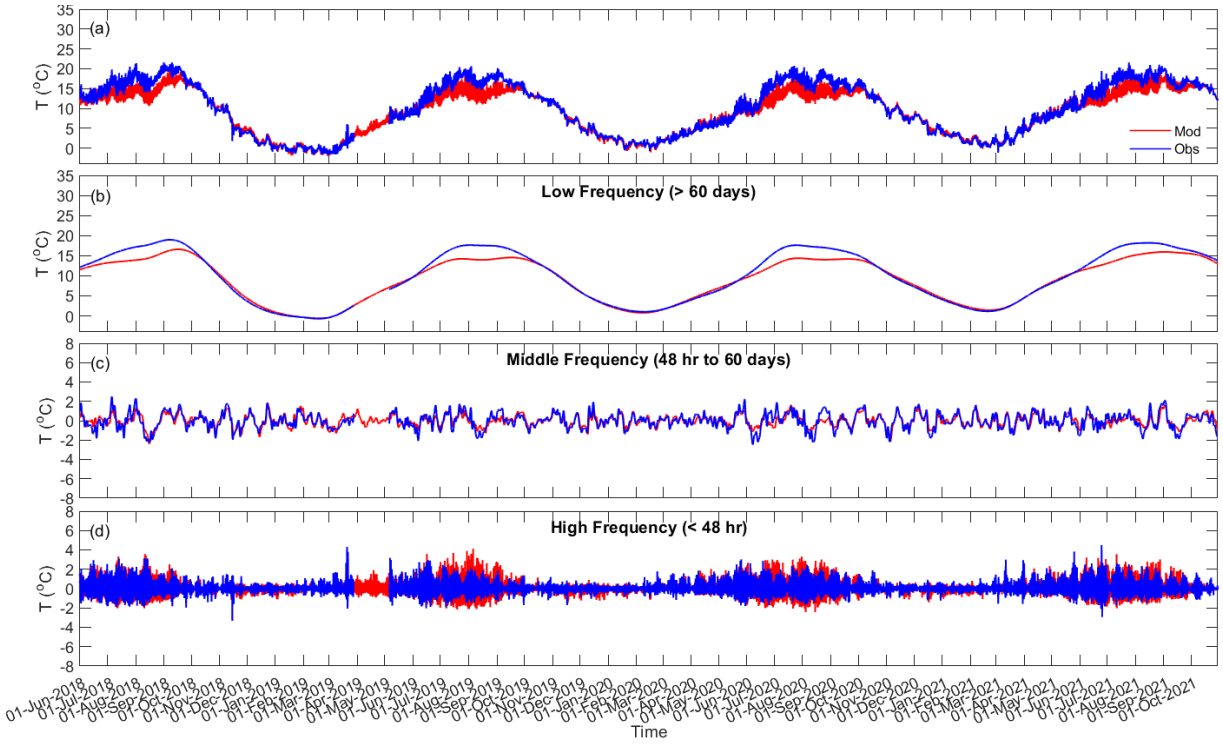

Fig. S3 At Mason's Island, bottom water (~10 cm above the bed) temperature time series (a), and time series of the bottom water temperature in low (> 60 days (seasonal band); b), middle (48 hr to 60 days (meteorological band); c), and high (< 48 hr; d) frequencies from observation data (blue) and model results (red).

836

837

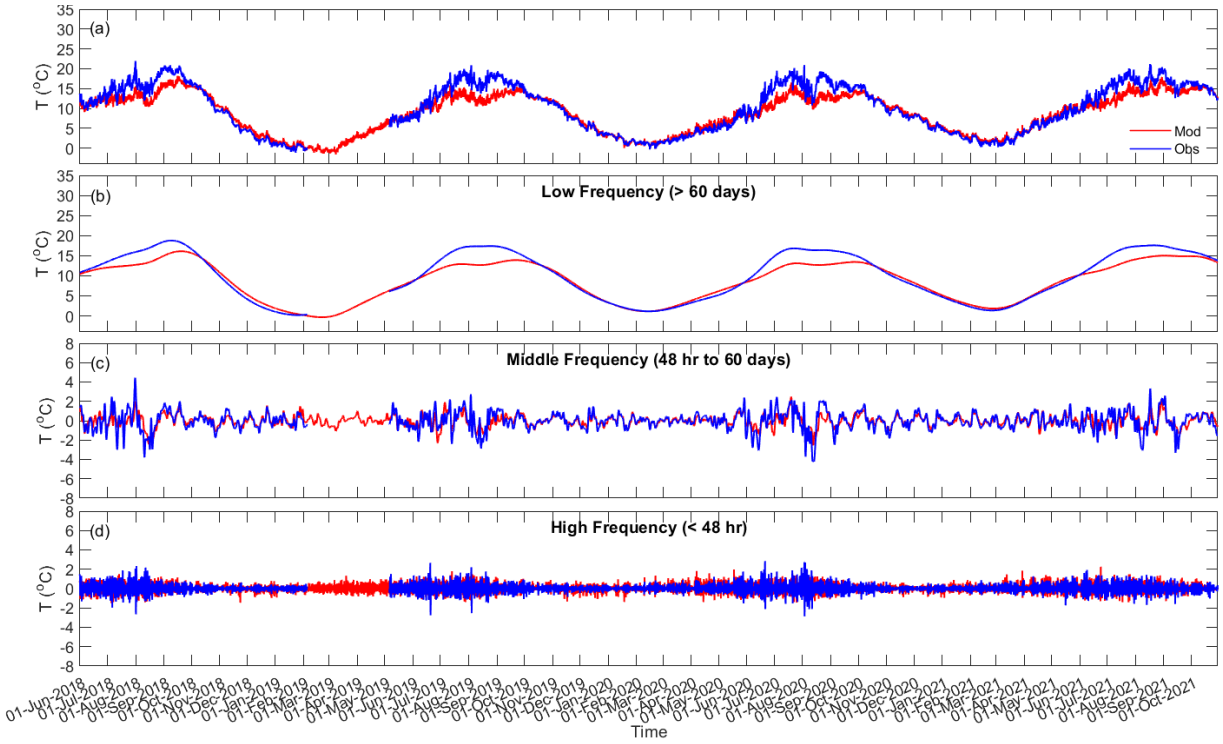

Fig. S4 At Sacrifice Island, bottom water (~10 cm above the bed) temperature time series (a), and time series of the bottom water temperature in low (> 60 days (seasonal band); b), middle (48 hr to 60 days (meteorological band); c), and high (< 48 hr; d) frequencies from observation data (blue) and model results (red).

838

839

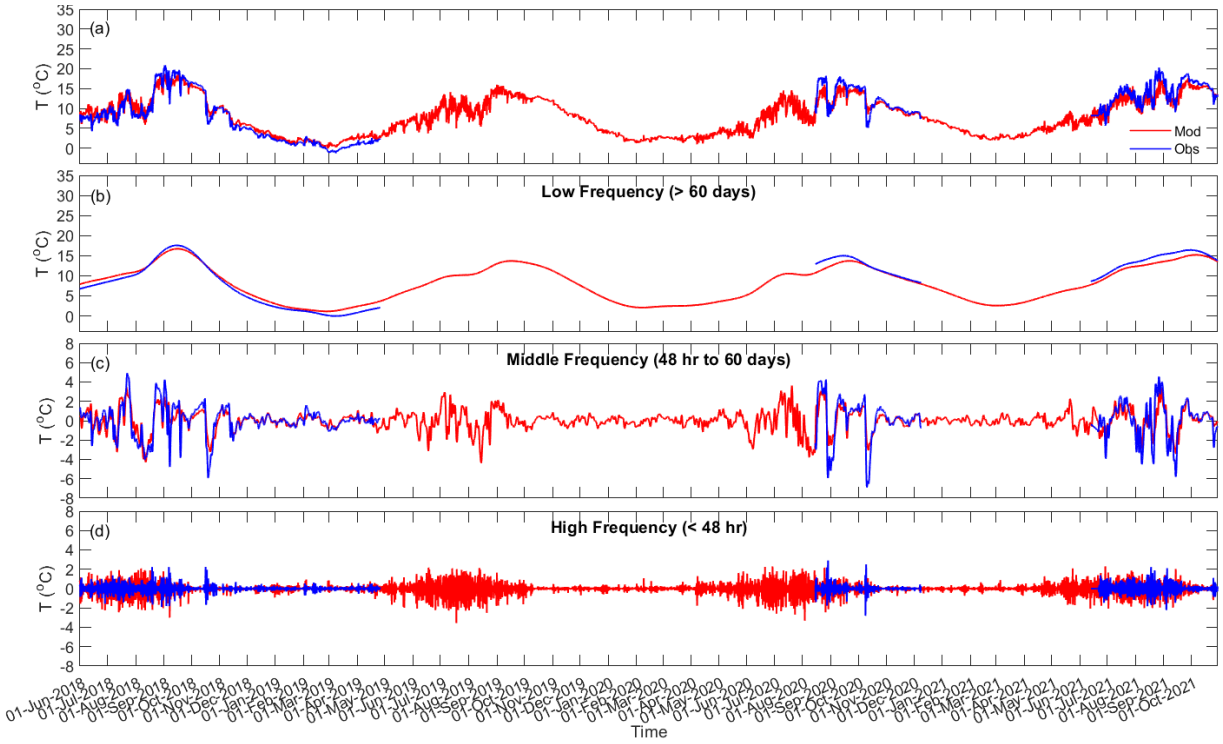

Fig. S5 At Sambro, bottom water (~10 cm above the bed) temperature time series (a), and time series of the bottom water temperature in low (> 60 days (seasonal band); b), middle (48 hr to 60 days (meteorological band); c), and high (< 48 hr; d) frequencies from observation data (blue) and model results (red).

840

841

842

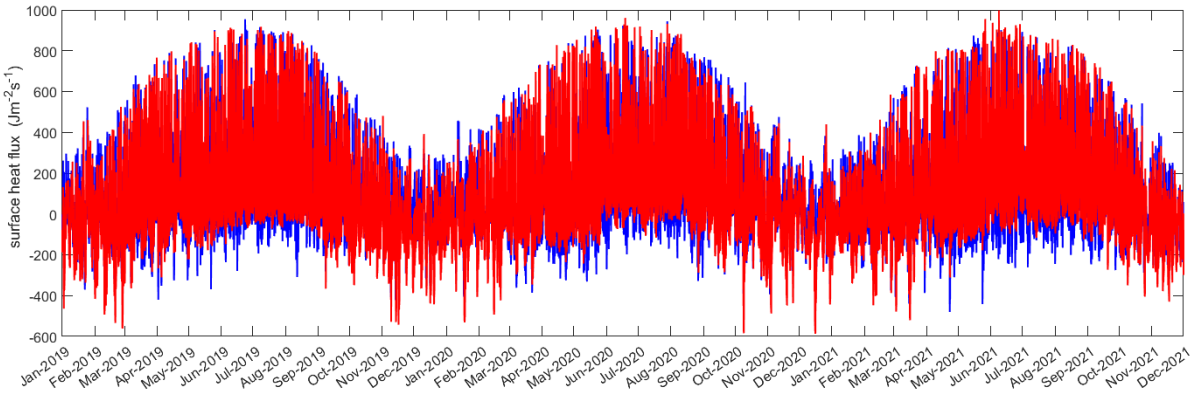

Fig. S6 Time series of the hourly surface heat flux per unit area at Port l'Hebert (blue) and Taylor Head (red).

843

844

845